Nonspinning black hole-neutron star mergers: a model for the amplitude of gravitational waveforms

Francesco Pannarale,[1,*] Emanuele Berti,[2,3,†] Koutarou Kyutoku,[4,‡] and Masaru Shibata[5,§]

[1] *Max-Planck-Institut für Gravitationsphysik, Albert Einstein Institut, Potsdam, Germany*
[2] *Department of Physics and Astronomy, The University of Mississippi, University, MS 38677, USA*
[3] *California Institute of Technology, Pasadena, CA 91109, USA*
[4] *Department of Physics, University of Wisconsin-Milwaukee, P.O.Box 413, Milwaukee, Wisconsin 53201, USA*
[5] *Yukawa Institute for Theoretical Physics, Kyoto University, Kyoto 606-8502, Japan*

(Dated: July 22, 2013)

Black hole-neutron star binary mergers display a much richer phenomenology than black hole-black hole mergers, even in the relatively simple case – considered in this paper – in which both the black hole and the neutron star are nonspinning. When the neutron star is tidally disrupted, the gravitational wave emission is radically different from the black hole-black hole case and it can be broadly classified in two groups, depending on the spatial extent of the disrupted material. We present a phenomenological model for the gravitational waveform amplitude in the frequency domain that encompasses the three possible outcomes of the merger: no tidal disruption, "mild", and "strong" tidal disruption. The model is calibrated to general relativistic numerical simulations using piecewise polytropic neutron star equations of state. It should prove useful to extract information on the nuclear equation of state from future gravitational-wave observations, and also to obtain more accurate estimates of black hole-neutron star merger event rates in second- and third-generation interferometric gravitational-wave detectors. We plan to extend and improve the model as longer and more accurate gravitational waveforms become available, and we will make it publicly available online as a *Mathematica* package. We also present in appendix analytical fits of the projected KAGRA noise spectral density, that should be useful in data analysis applications.

PACS numbers: 04.25.dk, 97.60.Jd, 97.60.Lf, 04.30.-w

I. INTRODUCTION

Numerical relativity has made impressive strides in the past couple of decades. Several research groups can now simulate the late inspiral and merger of compact binaries, which are the main target for second- and third-generation gravitational-wave (GW) detectors, such as Advanced LIGO/Virgo [1], KAGRA [2, 3], LIGO-India [4] and the Einstein Telescope [5]. These systems are composed of either black holes (BHs) or neutron stars (NSs), and they belong to three families: BH-BH, NS-NS, and BH-NS binaries. In general, the calculations are resource intensive and time consuming, so fully numerical simulations covering many cycles and spanning the whole parameter space of these binaries – including masses, spins, nuclear equation of state (EOS), etcetera – are still beyond the reach of present-day computers.

For this reason, semianalytical waveform models are necessary to bridge the gap between the early inspiral (where the binary dynamics can be treated via perturbative methods) and the merger phase. Analytical models covering the full inspiral and merger have several applications. First and foremost, they can be used to reduce the computational cost of building GW detection templates. The community has engaged in large-scale efforts, such as the NINJA/NINJA-2 and NRAR collaborations [6, 7], to optimize the task of injecting waveforms in detector data and of constructing matched-filtering templates. Semianalytical merger models are also valuable to improve event rate estimates, which are currently based on rather rough approximations to the actual binary waveforms [8, 9]: see e.g. [10, 11] for preliminary efforts in this direction. Last but not least (and more ambitiously), semianalytical models incorporating the characteristic signatures predicted by numerical merger simulations may prove useful, in conjunction with population synthesis models, to constrain the properties of compact binaries and the astrophysical formation scenarios leading to their formation. For example, Read *et al.* [12, 13] analyzed general relativistic simulations of NS-NS mergers to show that EOS information can be extracted (at least in principle) from departures from the point-particle limit of the gravitational waveform produced during the late inspiral. Bauswein *et al.* [14] used a three-dimensional relativistic smoothed-particle hydrodynamics code to demonstrate a correlation between the NS radii and the peak frequency of the postmerger GW signal from NS-NS mergers. Finally, Lackey *et al.* [15, 16] recently studied GW constraints on the NS EOS for BH-NS binaries using a Fisher matrix analysis of hybrid waveforms obtained by combining either post-Newtonian (PN) or effective-one-body (EOB) models with numerical waveforms.

* francesco.pannarale@aei.mpg.de
† berti@phy.olemiss.edu
‡ kyutoku@uwm.edu
§ mshibata@yukawa.kyoto-u.ac.jp

It is fair to state that semianalytical models and numerical simulations are most advanced for BH-BH systems. Phenomenological waveform models spanning inspiral, merger, and ringdown (IMR) were initially proposed by Ajith *et al.* for nonspinning binaries [17–19], and later extended to spinning, nonprecessing binaries [20]. The original (nonspinning) and improved (spinning) versions of this model are sometimes referred to as "PhenomA" [18] and "PhenomB" [20], or alternatively as "PhenV1" and "PhenV2": see e.g. [21]. An upgraded version of these models was subsequently proposed by Santamaría *et al.* [22]: this last model is sometimes called "PhenomC" or "PhenV3", and it has the important feature of reducing by construction to the correct PN limit in the early inspiral. Progress in tuning the EOB model to numerical BH-BH simulations has also been remarkable: see e.g. [23, 24] for the latest incarnations of these models, and [21, 25] for comparisons between waveforms of the EOB and PhenomX (X=A, B, C) families.

Phenomenological BH-BH waveforms have been extensively used in parameter estimation studies. PhenomX waveforms were used in data analysis applications for both Earth-based [26] and space-based detectors [27–30]. Systematic errors in parameter estimation are likely to be important, but there are relatively few studies in this direction. For example, PN waveforms were used to quantify errors in estimating full IMR PhenomA waveform parameters in [31], while systematic errors of EOB models in the LISA context were investigated in [32]. Parameter estimation accuracy and systematic errors depend mostly on GW phasing, which relies on long and accurate simulations. Such long and accurate simulations are particularly hard to achieve for compact binaries containing NSs. For NS-NS or BH-NS binaries (unlike BH-BH binaries) the outcome of the merger depends on several physical assumptions (e.g. on the nuclear EOS, magnetic fields, neutrino emission, and so on) that are currently poorly constrained by laboratory experiments and astrophysical observations. General relativistic simulations of NS-NS mergers, however, have been studied for a long time, and they are now long and accurate enough to be compared with analytical models. These studies hold the promise to constrain the EOS of matter at supranuclear densities, e.g. via the measurement of tidal deformation parameters: see e.g. [12, 13, 33–36] for recent studies.

For BH-NS systems, present simulations are comparatively short. Difficulties arise because BH-NS binaries are expected to have relatively large mass ratio, which causes complications for both analytical and numerical approaches. For typical values of the BH-NS mass ratio, the convergence of the PN approximation is expected to be slower than in the NS-NS case (see e.g. [37] for a systematic study in the context of initial data). On the other hand, numerical codes must track very different dynamical timescales, making simulations heavily resource intensive. Recent investigations [38, 39] studied the impact of precession and of different PN approximants on the detection of BH-NS binary inspirals. The state of the art for gravitational waveform modeling includes an attempt to incorporate higher harmonics in the inspiral signal [40], and recent work (involving some of us) on the construction of hybrid waveforms to measure EOS parameters from BH-NS mergers [16].

An important caveat in building phenomenological models is that BH-NS simulations are still too short to guarantee accurate phasing estimates in the whole parameter space. Therefore, in this paper we adopt a conservative approach and focus on the analytical modeling of the GW *amplitude* in the frequency domain. For consistency and continuity with previous studies, we find it convenient to build our GW amplitude model on the foundations of the BH-BH PhenomC model [22]. Additional parameters needed to reproduce the complex phenomenology of BH-NS systems are introduced and tuned using the simulations reported in [15, 41]. Our main interest here is to reproduce the high-frequency behavior of the GW spectrum reported in these simulations, where most of the interesting EOS-related phenomenology takes place. We will show that our model is useful to improve signal-to-noise-ratio (SNR) estimates for BH-NS systems (which depend only on the GW amplitude in the frequency domain) and to obtain estimates of the cutoff frequency of the merger signal – a potentially measurable quantity – in different physical scenarios. The model can (and will) be improved as longer, more accurate simulations become available.

The plan of the paper is as follows. In Sec. II we anticipate our main results and provide a concise recipe to implement our model. Section III reviews the numerical simulations used to calibrate and verify the model, and Sec. IV illustrates the logic we followed to build the BH-NS model upon the BH-BH PhenomC model. In Sec. V we compare our model of GW spectra with all binaries for which we have numerical data, in order to validate it and test its accuracy. In Sec. VI we compare SNRs obtained for BH-NS binaries when using our model, the PhenomC model, and the commonly employed restricted PN approximation. We use different noise curves and conclude that while the use of numerical waveforms can induce SNR corrections as large as $\sim 10\%$ with respect to the "standard" restricted PN approximation, BH-BH phenomenological models are accurate enough to compute the SNR even when used to model (nonspinning) BH-NS mergers. In Sec. VII we use our model to compute the cutoff frequency of the merger signal in the three different physical scenarios (no tidal disruption, mild tidal disruption, and strong tidal disruption). These results could find application in theoretical calculations of tidal disruption, which in turn can be used to assess the detectability of EOS effects in BH-NS mergers. Appendix A clarifies the relation between different conventions on the waveform amplitude used in the literature. Finally, Appendix B provides (to our knowledge, for the first time) analytical fits to different proposed KAGRA noise curves [3]. Throughout the paper, unless specified otherwise, we use geometrical units ($G = c = 1$).

II. EXECUTIVE SUMMARY OF THE INSPIRAL-MERGER-RINGDOWN MODEL

We begin this paper by summarizing our model for the frequency-domain GW amplitude. This section is essentially a step-by-step recipe to facilitate the implementation (and possibly improvement) of the model in SNR calculations and data analysis codes. We begin by reviewing the BH-BH PhenomC construction, and then list the modifications of PhenomC that are necessary in order to reproduce the more complex phenomenology of nonspinning BH-NS mergers.

A. The black hole-black hole merger model

The BH-BH PhenomC waveforms of [22] are built in the frequency domain, which is particularly convenient for SNR calculations. In this section, unless otherwise noted and in accordance with the conventions of [22], all frequencies are to be intended as multiplied by the sum $m_0 = M_1 + M_2$ of the two initial BH masses (in other words, we are using units in which $m_0 = 1$). The amplitude $\tilde{A}_{\rm Phen}(f)$ of the frequency-domain signal $\tilde{h}_{\rm Phen}(f) = \tilde{A}_{\rm Phen}(f) e^{i\Phi_{\rm Phen}}$ is split in a sum of two terms:

$$\tilde{A}_{\rm Phen}(f) = \tilde{A}_{\rm PM}(f) w^-_{f_0,d}(f) + \tilde{A}_{\rm RD}(f) w^+_{f_0,d}(f)\,. \quad (1)$$

Here $\tilde{A}_{\rm PM}(f)$ models the inspiral and premerger amplitude, and in turn it is decomposed in a sum of the form

$$\tilde{A}_{\rm PM}(f) = \tilde{A}_{\rm PN}(f) + \gamma_1 f^{5/6}\,, \quad (2)$$

where the first term is a PN inspiral contribution (the coefficients of which are collected in the Appendix of [22]), and the second term is intended to model premerger (strong-field) modifications to the PN inspiral. The amplitude γ_1 of this second contribution is fitted to BH-BH hybrid waveform data.

The second term of Eq. (1),

$$\tilde{A}_{\rm RD}(f) = \delta_1 \mathcal{L}(f, f_{\rm RD}(\chi_{\rm f}, m_0), \delta_2 \mathcal{Q}(\chi_{\rm f})) f^{-7/6}\,, \quad (3)$$

is the ringdown amplitude, modeled with a Lorentzian $\mathcal{L}(f, f_0, \sigma) \equiv \sigma^2/[(f-f_0)^2 + \sigma^2/4]$. The ringdown amplitude, δ_1, is fitted to BH-BH hybrid waveform data, and so is δ_2, which accounts for inaccuracies in the fit (taken from [42]) used to calculate the remnant BH spin parameter $\chi_{\rm f}$. The remnant spin, $\chi_{\rm f}$, is used to determine the $l = m = 2$, $n = 0$ (later 220, for brevity) quasinormal mode (QNM) ringdown frequency, $f_{\rm RD}$, and quality factor, $\mathcal{Q}$, of the BH remnant, using the fitting formula provided in [43]. This ringdown frequency $f_{\rm RD}$ also depends on the mass of the BH remnant, which is approximated to m_0. Finally, $w^\pm_{f_0,d}(f)$ are the windowing functions

$$w^\pm_{f_0,d}(f) \equiv \frac{1}{2}\left[1 \pm \tanh\left(\frac{4(f-f_0)}{d}\right)\right]\,, \quad (4)$$

where the PhenomC model for BH-BH binaries sets $f_0 = 0.98 f_{\rm RD}$ and $d = 0.015$.

Summarizing, we have an IMR amplitude model for BH-BH gravitational waveforms in the frequency-domain which contains: (1) a PN contribution from the inspiral, (2) a premerger term with amplitude γ_1 fitted to BH-BH hybrid waveforms, and (3) a ringdown term given by a Lorentzian with overall amplitude set by the coefficient δ_1 and a second fitting coefficient δ_2 (which accounts for errors in the fit to $\chi_{\rm f}$). All of these coefficients are determined empirically by comparison with BH-BH hybrid waveforms.

B. The black hole-neutron star model: the algorithm, step by step

In order to generalize the PhenomC model [22], we start by writing the frequency-domain GW amplitude of BH-NS mergers in a similar way, i.e. as a sum of three terms:

$$\begin{aligned}\tilde{A}_{\rm Phen}(f) = {} & \tilde{A}_{\rm PN}(f) w^-_{\epsilon_{\rm ins}\tilde{f}_0, d+\sigma_{\rm tide}} \\ & + 1.25\gamma_1 f^{5/6} w^-_{\tilde{f}_0, d+\sigma_{\rm tide}} \\ & + \tilde{\mathcal{A}}_{\rm RD}(f) w^+_{\tilde{f}_0, d+\sigma_{\rm tide}}\,. \end{aligned} \quad (5)$$

Here the PN inspiral contribution $\tilde{A}_{\rm PN}(f)$, the premerger amplitude γ_1 and the parameter $d = 0.015$ are identical to those used in [22]. The ringdown amplitude is

$$\tilde{\mathcal{A}}_{\rm RD}(f) = \epsilon_{\rm tide}\delta_1 \mathcal{L}(f, f_{\rm RD}(\chi_{\rm f}, M_{\rm f}), \alpha\delta_2 \mathcal{Q}(\chi_{\rm f})) f^{-7/6}\,, \quad (6)$$

where the coefficients δ_1 and δ_2 are again calculated according to the fits reported in [22]. However, we also introduce the correction parameters $\epsilon_{\rm ins}$, $\sigma_{\rm tide}$, $\epsilon_{\rm tide}$, and α, and replace f_0 with $\tilde{f}_0$. The first three parameters and $\tilde{f}_0$ tend to 1, 0, 1, and f_0 (respectively) in the BH-BH limit, so that one recovers the binary BH model of [22]. The parameter α and the factor of 1.25 appearing in Eq. (5) are in apparent discrepancy with the BH-BH limit, and we discuss them at length below. In short, we believe that longer and more accurate comparisons of BH-NS and BH-BH waveforms generated by different codes are required to clarify the role of these parameters.

Given a BH-NS system formed by a nonspinning BH with gravitational mass $M_{\rm BH}$ and a nonspinning NS with gravitational mass $M_{\rm NS}$, baryonic mass $M_{\rm b,NS}$, radius $R_{\rm NS}$, and compactness $\mathcal{C} = M_{\rm NS}/R_{\rm NS}$ (where all of these quantities refer to BHs or NSs *in isolation*), the recipe to use Eq. (5) is the following:

1. Determine the coefficients γ_1, δ_1, and δ_2 using the BH-BH fits provided in [22].

2. Determine the correction α to δ_2 according to the fit in Eq. (28) below, where $\nu = M_{\rm BH}M_{\rm NS}/(M_{\rm BH} + M_{\rm NS})^2$ denotes the symmetric mass ratio.

3. Solve the equation

$$\frac{M_{\rm NS}\xi_{\rm tide}^3}{M_{\rm BH}} = \frac{3[\xi_{\rm tide} - 2(M_{\rm BH}/R_{\rm NS})]}{\xi_{\rm tide} - 3(M_{\rm BH}/R_{\rm NS})} \tag{7}$$

for $\xi_{\rm tide}$, a coefficient providing relativistic corrections to the standard Newtonian estimate of the orbital radius at *mass-shedding*: cf. Eq. (7) of [44], which in turn builds upon classic results by [45]. Then use this quantity to calculate the mass of the torus remaining around the NS at late times, $M_{\rm b,torus}$, according to the fitting formula [44]

$$\frac{M_{\rm b,torus}}{M_{\rm b,NS}} = 0.296\xi_{\rm tide}(1-2\mathcal{C}) - 0.171\frac{r_{\rm ISCO}}{R_{\rm NS}}\,, \tag{8}$$

where $r_{\rm ISCO}$ is the radius of the innermost stable circular orbit (ISCO) of the initial BH: see [46] and Eqs. (13) below.

4. Calculate the spin parameter $\chi_{\rm f}$ and gravitational mass $M_{\rm f}$ of the BH remnant, following the model of [47]. This requires solving numerically for $\chi_{\rm f}$ the closed expression

$$\chi_{\rm f} = \frac{l_z(\bar{r}_{\rm ISCO,f},\chi_{\rm f})M_{\rm BH}\{f(\nu)M_{\rm b,NS} + [1-f(\nu)]M_{\rm NS} - M_{\rm b,torus}\}}{[m_0\{1-[1-e(\bar{r}_{\rm ISCO,i},0)]\nu\} - e(\bar{r}_{\rm ISCO,f},\chi_{\rm f})M_{\rm b,torus}]^2}\,, \tag{9}$$

where $M = M_{\rm BH} + M_{\rm NS}$,

$$f(\nu) = \begin{cases} 0 & \nu \le 0.16 \\ \frac{1}{2}\left[1-\cos\left(\frac{\pi(\nu-0.16)}{2/9-0.16}\right)\right] & 0.16 < \nu < 2/9 \\ 1 & \nu \ge 2/9 \end{cases} \tag{10}$$

and $l_z(\bar{r},\chi)$ and $e(\bar{r},\chi)$ denote the angular momentum and energy per unit mass of a point particle on a circular orbit of radius $\bar{r}$ around a Kerr BH of unit mass and dimensionless spin parameter χ. They are given by the expressions

$$e(\bar{r},\chi) = \frac{\bar{r}^2 - 2\bar{r} \pm \chi\sqrt{\bar{r}}}{\bar{r}(\bar{r}^2 - 3\bar{r} \pm 2\chi\sqrt{\bar{r}})^{1/2}}\,, \tag{11}$$

$$l_z(\bar{r},\chi) = \pm\frac{\bar{r}^2 \mp 2\chi\sqrt{\bar{r}} + \chi^2}{\sqrt{\bar{r}}(\bar{r}^2 - 3\bar{r} \pm 2\chi\sqrt{\bar{r}})^{1/2}}\,, \tag{12}$$

whereas the ISCO radii are calculated according to

$$\begin{aligned} \bar{r}_{\rm ISCO} &= [3 + Z_2 \mp \sqrt{(3-Z_1)(3+Z_1+2Z_2)}]\,, \\ Z_1 &= 1 + (1-\chi^2)^{1/3}\left[(1+\chi)^{1/3} + (1-\chi)^{1/3}\right]\,, \\ Z_2 &= \sqrt{3\chi^2 + Z_1^2}\,. \end{aligned} \tag{13}$$

The upper/lower sign holds for prograde/retrograde orbits [46]. Once $\chi_{\rm f}$ is determined, $M_{\rm f}$ follows from

$$\begin{aligned} M_{\rm f} = {} & m_0\{1-[1-e(\bar{r}_{\rm ISCO,i},0)]\nu\} \\ & - M_{\rm b,torus}e(\bar{r}_{\rm ISCO,f},\chi_{\rm f})\,. \end{aligned} \tag{14}$$

5. Compute the GW reference frequency for the *onset* of the NS tidal disruption:

$$f_{\rm tide} = \pm\frac{1}{\pi(\chi_{\rm f}M_{\rm f} + \sqrt{\tilde{r}_{\rm tide}^3/M_{\rm f}})}\,, \tag{15}$$

where the orbital radius at the onset of tidal disruption is

$$\tilde{r}_{\rm tide} = \xi_{\rm tide}R_{\rm NS}(1-2\mathcal{C})\,. \tag{16}$$

6. Use $\chi_{\rm f}$ and $M_{\rm f}$ to determine the 220 ringdown frequency $f_{\rm RD}$ and quality factor $\mathcal{Q}$ of the BH remnant, that is, following the fits of [43], calculate

$$f_{\rm RD} = [1.5251 - 1.1568(1-\chi_{\rm f})^{0.1292}]/(2\pi M_{\rm f})\,, \tag{17}$$

$$\mathcal{Q} = 0.700 + 1.4187(1-\chi_{\rm f})^{0.4990}\,. \tag{18}$$

7. Set

$$\tilde{f}_0 = \min[f_{\rm tide}, \tilde{f}_{\rm RD}]\,, \tag{19}$$

where $\tilde{f}_{\rm RD} \equiv 0.99 \times 0.98 f_{\rm RD}$.

8a. If $\tilde{f}_0 = \tilde{f}_{\rm RD}$, then the merger is "nondisruptive", and the NS matter accretion is coherent until the plunge, so the merger and the pure inspiral contributions to Eq. (25) end at the same frequency, i.e. $\epsilon_{\rm ins} = 1$. $\epsilon_{\rm tide}$ and $\sigma_{\rm tide}$ are instead determined according to the fits of Sec. IV B 1.

8b. If $\tilde{f}_0 = f_{\rm tide}$ and $M_{\rm b,torus} > 0$, then the merger is "disruptive", the NS material is scattered around, and the ringdown contribution to Eq. (25) vanishes, i.e. $\epsilon_{\rm tide} = 0$. $\epsilon_{\rm ins} \neq 1$ and $\sigma_{\rm tide} \neq 0$ are determined according to the fits of Sec. IV B 2.

8c. If $\tilde{f}_0 = f_{\rm tide}$ and $M_{\rm b,torus} = 0$, then the merger is "mildly disruptive". The parameter $\epsilon_{\rm ins}$ is found as for the disruptive cases, while $\epsilon_{\rm tide}$ is determined as for the nondisruptive cases, i.e. the shutoff of the signal has an intermediate behavior between a tidal disruption shutoff and a QNM ringdown. $\sigma_{\rm tide}$ takes the value 0.041.

In Sec. III below we will review the numerical simulations used to calibrate this model. Then, in Sec. IV we will clarify how physical intuition on tidal disruption was used to build the model itself.

III. THE NUMERICAL SIMULATIONS

The numerical simulations used to calibrate our model adopt piecewise polytropic EOSs, which are meant to reproduce nuclear-theory based EOSs with a small number of polytropic constants κ_i and exponents Γ_i [48]:

$$P(\rho) = \kappa_i \rho^{\Gamma_i} \quad \text{for} \quad \rho_{i-1} \leq \rho < \rho_i \quad (i = 1 \ldots, n)\,. \tag{20}$$

Since the pressure is required to be continuous, i.e.

$$\kappa_i \rho_i^{\Gamma_i} = \kappa_{i+1} \rho_i^{\Gamma_{i+1}}\,, \tag{21}$$

the EOS is completely specified once we assign κ_1, Γ_i and ρ_i $(i = 1 \ldots, n)$. More specifically, we consider a two-region piecewise polytrope[1]. We set the "crustal" polytropic parameters to be $\Gamma_1 = 1.35692395$ and $\kappa_1/c^2 = 3.99873692 \times 10^{-8} ({\rm g/cm^3})^{1-\Gamma_1}$, and we vary Γ_2. Instead of specifying ρ_1 we assign the pressure $P_{\rm fidu}$ at the fiducial density $\rho_{\rm fidu} = 10^{14.7}$ g/cm^3, because this parameter is correlated with the NS radius. The relations

$$P_{\rm fidu} = \kappa_2 \rho_{\rm fidu}^{\Gamma_2}\,, \quad \kappa_1 \rho_1^{\Gamma_1} = \kappa_2 \rho_1^{\Gamma_2}\,, \tag{22}$$

then determine the values of κ_2 and ρ_1.

The numerical runs used to build and test our model are collected in Tables I and II. The beginning of each run name identifies the NS EOS, following the naming scheme for piecewise polytropes introduced in [12, 41, 48]. In particular, 2H, 1.5H, 1.25H, H, HB, and B denote EOSs with the same value of the core polytropic exponent $\Gamma_2 =$

TABLE I. Physical parameters of the numerical-relativity simulations used to develop the waveform model [15, 41]. The pressure at the fiducial density $10^{14.7}$g/cm^3 is in dyne/cm^3, whereas the NS mass is in solar masses.

Run Label	Γ_2	$\log P_{\rm fidu}$	$M_{\rm NS}$	$\mathcal{C}$	Q	$\chi_{\rm i}$
B-M135-Q5	3.0	34.3	1.35	0.1819	5	0
H-M135-Q5	3.0	34.5	1.35	0.1624	5	0
2H-M135-Q5	3.0	34.9	1.35	0.1309	5	0
B-M135-Q4	3.0	34.3	1.35	0.1819	4	0
H-M135-Q4	3.0	34.5	1.35	0.1624	4	0
2H-M135-Q4	3.0	34.9	1.35	0.1309	4	0
B-M135-Q3	3.0	34.3	1.35	0.1819	3	0
HB-M135-Q3	3.0	34.4	1.35	0.1718	3	0
H-M135-Q3	3.0	34.5	1.35	0.1624	3	0
2H-M135-Q3	3.0	34.9	1.35	0.1309	3	0
B-M135-Q2	3.0	34.3	1.35	0.1819	2	0
HB-M135-Q2	3.0	34.4	1.35	0.1718	2	0
H-M135-Q2	3.0	34.5	1.35	0.1624	2	0
2H-M135-Q2	3.0	34.9	1.35	0.1309	2	0

TABLE II. Physical parameters of the numerical-relativity simulations used to test the waveform model and assess its validity beyond the runs used to build it (see Table I for additional information). The three groups of runs allow us to test the model for different values of $M_{\rm NS}$, $\log P_{\rm fidu}$ (for $\Gamma_2 = 3.0$), and Γ_2, respectively.

Run Label	Γ_2	$\log P_{\rm fidu}$	$M_{\rm NS}$	$\mathcal{C}$	Q	$\chi_{\rm i}$
B-M12-Q2	3.0	34.3	1.20	0.1614	2	0
HB-M12-Q2	3.0	34.4	1.20	0.1527	2	0
H-M12-Q2	3.0	34.5	1.20	0.1447	2	0
2H-M12-Q2	3.0	34.9	1.20	0.1172	2	0
1.5H-M135-Q5	3.0	34.7	1.35	0.1456	5	0
1.5H-M135-Q4	3.0	34.7	1.35	0.1456	4	0
1.5H-M135-Q3	3.0	34.7	1.35	0.1456	3	0
1.5H-M135-Q2	3.0	34.7	1.35	0.1456	2	0
1.25H-M135-Q2	3.0	34.6	1.35	0.1537	2	0
Bl-M135-Q2	3.3	34.3	1.35	0.1798	2	0
HBl-M135-Q2	3.3	34.4	1.35	0.1719	2	0
Hl-M135-Q2	3.3	34.5	1.35	0.1638	2	0
1.25Hl-M135-Q2	3.3	34.6	1.35	0.1565	2	0
1.5Hl-M135-Q2	3.3	34.7	1.35	0.1497	2	0
Bs-M135-Q2	2.7	34.3	1.35	0.1856	2	0
HBs-M135-Q2	2.7	34.4	1.35	0.1723	2	0
Hs-M135-Q2	2.7	34.5	1.35	0.1605	2	0
1.25Hs-M135-Q2	2.7	34.6	1.35	0.1497	2	0
1.5Hs-M135-Q2	2.7	34.7	1.35	0.1399	2	0
Bss-M135-Q2	2.4	34.3	1.35	0.1941	2	0
HBss-M135-Q2	2.4	34.4	1.35	0.1741	2	0
Hss-M135-Q2	2.4	34.5	1.35	0.1577	2	0
1.25Hss-M135-Q2	2.4	34.6	1.35	0.1435	2	0
1.5Hss-M135-Q2	2.4	34.7	1.35	0.1312	2	0

[1] Strictly speaking, some of our piecewise polytropic EOSs (Bss, Bs, HBss, HBs, and Hss) do not support the recent observations of NSs with mass $M_{\rm NS} \geq 2\,M_\odot$ [49, 50], but this does not necessarily mean that these EOS models are not realistic. The reason is that regions of very high density are not relevant for the BH-NS binaries studied here, where the NS typically has mass $M < 1.4\,M_\odot$; therefore we can conceivably modify the high-density EOS in order to satisfy observational constraints on the maximum mass without altering our conclusions on gravitational waveforms from BH-NS binaries.

3.0, but decreasing values of the pressure at the fiducial density $\log P_{\rm fidu} = \{34.9, 34.7, 34.6, 34.5, 34.4, 34.3\}$, so that 2H is the stiffest and B is the softest EOS in the group; an appended "l", "s", or "ss" means that the EOS has the same $\log P_{\rm fidu}$ but a different value of Γ_2 ("l" stands for larger and "s" for "smaller" core polytropic exponent, so $\Gamma_2 = 3.3$, 2.7, 2.4 for an EOS with appended "l", "s", or "ss", respectively). The rest of the name encodes the NS mass (e.g., M135 means that $M_{\rm NS} = 1.35 M_\odot$) and the binary mass ratio $Q \equiv M_{\rm BH}/M_{\rm NS}$.

Our simulations are such that the cases with $\Gamma_2 = 3.0$ span mass ratios $Q = \{2, 3, 4, 5\}$, whereas the cases with $\Gamma_2 = \{2.4, 2.7, 3.3\}$ all have $Q = 2$. If we were to use all the data we would run the risk of being biased by core stiffness effects for low BH masses. In this first paper, we therefore decided to build the IMR GW amplitude model on the runs with $\Gamma_2 = 3.0$ EOSs, which span all the available values of Q, and to leave the $Q = 2$, $M_{\rm NS} = 1.35 M_\odot$, $\Gamma_2 \neq 3$ ones (last part of Table II) as test cases to verify the validity of the model against variations of the NS core polytropic exponent. Further, we select a subset of $\Gamma_2 = 3.0$ simulations as additional test cases. These are 9 simulations: 4 with $M_{\rm NS} = 1.2 M_\odot$ (first block in Table II), and 5 with EOS 1.5H or 1.25H (second block in Table II). The reasoning behind this procedure is that once the model is built, we may test its validity against binaries with $M_{\rm NS} \neq 1.35 M_\odot$ and a subset of EOSs with $\Gamma_2 = 3.0$ that were not used to calibrate it. The $\Gamma_2 = 3.0$, 1.5H runs have the additional benefit of allowing us to test the model over different values of Q.

Once again, when more runs for $\Gamma_2 \neq 3.0$ and $Q \neq 2$ will be available, we plan to generalize the model so that the dependence on Γ_2 somehow appears explicitly. This may require using the NS Love numbers (as opposed to the NS compactness) in our expressions and fits used to determine the GW spectrum (cf. [16]).

IV. MODELING NONSPINNING BLACK HOLE-NEUTRON STAR WAVEFORMS

As discussed in Sec. II, the phenomenological coefficients γ_1, δ_1, and δ_2 appearing in the PhenomC model of [22] are fitted to BH-BH hybrid waveforms. It is natural to expect that these coefficients should be somehow corrected in a BH-NS binary model. A second aspect one may a priori envisage to modify, in the spirit of the PhenomC model, is the connection between the inspiral and premerger phases, which in the BH-BH case are "turned off" together using a unique windowing function $w^-_{f_0,d}$. In the PhenomC model the $\gamma_1 f^{5/6}$ term of Eq. (1) is supposed to represent the merger contribution to the amplitude, so we should somehow separate it from $\tilde{A}_{\rm PN}(f)$ in the case of mixed binaries: the NS can be elongated and disrupted prior to merger, so the behavior of a BH-NS premerger can differ significantly from the BH-BH case. These considerations lead us to the following generalization of the amplitude model in Eq. (1):

$$\begin{aligned}\tilde{A}_{\rm Phen}(f) = &\tilde{A}_{\rm PN}(f) w^-_{f_1,d_1} \\ &+ \kappa \gamma_1 f^{5/6} w^-_{f_2,d_3} \\ &+ \tilde{\mathcal{A}}_{\rm RD}(f) w^+_{f_3,d_3}\,, \end{aligned} \tag{23}$$

where we explicitly wrote down three different frequencies and widths for the windowing functions, and we introduced a correction κ to the BH-BH coefficient γ_1. For ease of comparison, we choose to model the PN contribution $\tilde{A}_{\rm PN}(f)$ using the same PN approximation for the inspiral as in [22], i.e. we neglect tidal effects on the GW amplitude of the inspiral (see e.g. [34, 41, 51] for recent studies of the influence of tidal effects in the late inspiral). The ringdown amplitude, $\tilde{\mathcal{A}}_{\rm RD}$, is now modified as explained in Eq. (6). Once more, the functional form is similar to the $\tilde{A}_{\rm RD}$ used in the model of [22], but the BH-BH fitted quantities δ_1 and δ_2 are corrected by two new "fudge factors" $\epsilon_{\rm tide}$ and α, respectively. Both parameters play a physical role: $\epsilon_{\rm tide}$ tends to unity when the BH-NS coalescence shows no or little tidal effects and has a very BH-BH-like behavior, and vice versa it tends to zero when tidal effects take over (so that the ringdown of the BH remnant is excited less and less). As we will see shortly, α takes care of the fact that in our model we allow the mass of the BH remnant in a BH-NS merger to be different from $M_{\rm BH} + M_{\rm NS}$ (at variance with [22]); it also compensates for using the BH-NS model of [47], rather than the BH-BH model of [42], in our prediction of the final spin $\chi_{\rm f}$.

When the BH-NS coalescence is nondisruptive, this generalization should reduce to Eq. (1). Furthermore, the three IMR contributions should be connected smoothly. In order to satisfy these constraints we set

$$d_i = d + \sigma_{\rm tide}\,, \tag{24}$$

where $d = 0.015$ is the BH-BH windowing width and $\sigma_{\rm tide}$ is a tidal (or finite-size) correction to d, which must tend to zero as NS tidal distortions become weaker. Next, and again for smoothness and continuity reasons, we set $f_2 = f_3$. For physical reasons, we also impose $f_1 \leq f_2$: this means that the ending frequency of the "pure" inspiral contribution should never be larger than the ending frequency of the merger contribution. We expect that $f_1 \to f_2$ as the coalescence becomes more and more BH-BH-like and tidal effects become more and more negligible, so we write $f_1 = \epsilon_{\rm ins} f_2$, with $0 < \epsilon_{\rm ins} \leq 1$.

All in all, we have

$$\begin{aligned}\tilde{A}_{\rm Phen}(f) = &\tilde{A}_{\rm PN}(f) w^-_{\epsilon_{\rm ins}\tilde{f}_0,d+\sigma_{\rm tide}} \\ &+ \kappa \gamma_1 f^{5/6} w^-_{\tilde{f}_0,d+\sigma_{\rm tide}} \\ &+ \tilde{\mathcal{A}}_{\rm RD}(f) w^+_{\tilde{f}_0,d+\sigma_{\rm tide}}\,, \end{aligned} \tag{25}$$

where we made the notational change $f_2 \to \tilde{f}_0$, hinting to the fact that this frequency should be close to the 220 QNM ringdown frequency of the BH remnant as tidal effects become smaller.

Eq. (25) is our general framework, and from now on we specify the details of our model. Let us begin by examining the BH remnant. In the case of the BH-BH phenomenological GW model in Eq. (1), the fit of [42] is used to predict the spin parameter $\chi_{\rm f}$ of the BH remnant, and its mass $M_{\rm f}$ is assumed to be equal to m_0. This enables one to calculate $f_{\rm RD}$ and $\mathcal{Q}$, which enter the ringdown amplitude model through $\tilde{A}_{\rm RD}$. This approach cannot reproduce all data for the BH remnant of BH-NS binary mergers accurately enough, as it is based on results of BH-BH merger simulations. We may use the model of [47] to predict $\chi_{\rm f}$ and $M_{\rm f}$ more accurately, but (as we briefly mentioned earlier) two caveats are necessary. First of all, in this case the mass of the BH remnant is not simply equal to $M_{\rm BH}+M_{\rm NS}$, and we expect this to generate some differences with the binary BH GW model introduced in [22]: the factor α that corrects the BH-BH fitted coefficient δ_2 and appears in Eq. (6) takes care of this, and also of the fact that $\chi_{\rm f}$ is predicted with the BH-NS model of [47] rather than the BH-BH model of [42]. Secondly, the approach of [47] relies on the prediction of [44] for the mass $M_{\rm b,torus}$ of the torus remnant (possibly) produced by a BH-NS coalescence. Reference [44] also provides a prediction for the orbital radius at the onset of tidal disruption, i.e. at mass-shedding. This is given in Eq. (16), where $\xi_{\rm tide}$ is the solution of Eq. (7). The prediction for $\tilde{r}_{\rm tide}$ relies on several approximations (e.g. it is coordinate dependent), but it may be usefully exploited in combination with the predictions for $\chi_{\rm f}$ and $M_{\rm f}$ to define a GW reference frequency as in Eq. (15). This is consistent with the calculation of $M_{\rm b,torus}$, and tends to infinity as $\mathcal{C}\to 1/2$ (that is, in the BH limit). In addition to writing out Eq. (25), we have thus chosen how to determine $\chi_{\rm f}$ and $M_{\rm f}$ (and hence how to calculate the $f_{\rm RD}$ and $\mathcal{Q}$ entering $\tilde{\mathcal{A}}_{\rm RD}$), and introduced the useful frequency $f_{\rm tide}$.

We then proceed by finding the values of κ, α, $\epsilon_{\rm tide}$, $\sigma_{\rm tide}$, $\epsilon_{\rm ins}$, and $\tilde{f}_0$ which best reproduce the high-frequency behavior of our numerical GW amplitude. As a final step, we must look for correlations between the values we found for κ, α, $\epsilon_{\rm tide}$, $\sigma_{\rm tide}$, $\epsilon_{\rm ins}$, and $\tilde{f}_0$, on one hand, and binary and remnant parameters, on the other.

In this study we focus on high frequencies for two reasons: (1) we are interested in the regime where the BH-NS phenomenology departs from the BH-BH case, and EOS-dependent effects emerge at high frequencies; (2) current simulations do not allow us to accurately handle the inspiral regime (for example, we do not make attempts to reduce the residual orbital eccentricity). In this regard, it is useful to remark that the influence of resolution on frequency-domain GW spectra was investigated in Fig. 15 of [41]. That study suggests that systematic errors due to resolution should be subdominant compared with effects due to (i) the finite length of the simulations, and (ii) the residual eccentricity of the initial data. These important aspects should be addressed with future, longer, and more accurate numerical simulations, that will presumably reduce the differences between the numerical data and the analytical PN-based description of the inspiral regime.

A. Black hole-black hole like mergers

Let us first consider a "BH-BH-like" mixed binary merger with the softest EOS, namely the $Q=5$ case with EOS B and $M_{\rm NS}=1.35M_\odot$ (`B-M135-Q5` in Table I). No torus is produced in this merger, and $f_{\rm tide}>f_{\rm RD}$. In Fig. 1 we show the numerical data for the GW spectrum (grey curve), the prediction of the PhenomC model of [22] (blue, dot-dashed curve), the prediction of the BH-NS model of Lackey and collaborators [16] (green, dotted curve), and the prediction of Eq. (25) with κ, α, $\epsilon_{\rm tide}$, $\sigma_{\rm tide}$, $\epsilon_{\rm ins}$, and $\tilde{f}_0$ tuned to mimic the high-frequency behavior of the numerical data (red, dashed curve). Throughout this paper, in the GW strain plots, we find it convenient to use the dimensionless frequency $m_0 f$, in place of f. As a reference for quick conversions between the two, the following formula may be used:

$$f = 2030\,{\rm Hz}\times\frac{m_0 f}{0.01}\frac{1}{\hat{M}_{\rm NS}(1+Q)}\,, \qquad (26)$$

where $\hat{M}_{\rm NS}$ is the NS mass in solar mass units. For example, for a system with mass ratio $Q=5$ and a NS of $1.35M_\odot$, $m_0 f=0.1$ corresponds to $\sim 2500\,$Hz.

Note that the initial match between the numerical data and the analytic spectra is not obtained "artificially" by rescaling the data to achieve the matching. It is, instead, obtained mathematically by a careful comparison of numerical and analytical conventions on the waveform

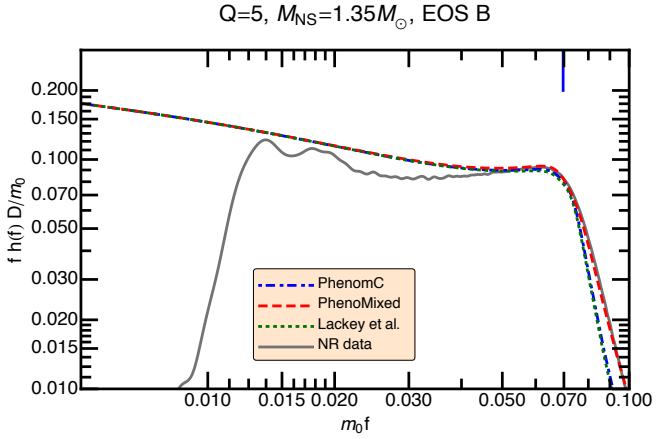

FIG. 1. GW amplitude of a BH-NS binary merger with a $1.35M_\odot$ NS with EOS B, a nonspinning BH, and a mass ratio $Q=5$ (Table I, `B-M135-Q5`). The GW strain of the NR simulation (continuous grey) is compared to the BH-BH phenomenological model of [22] (dot-dashed blue), to the BH-NS model of [16] (dotted green), and to our phenomenological model (dashed red). The location of $m_0\tilde{f}_{\rm RD}$ is shown by a short, blue, vertical line in the top of the graph; the mass-shedding frequency $m_0 f_{\rm tide}$ is higher than 0.1.

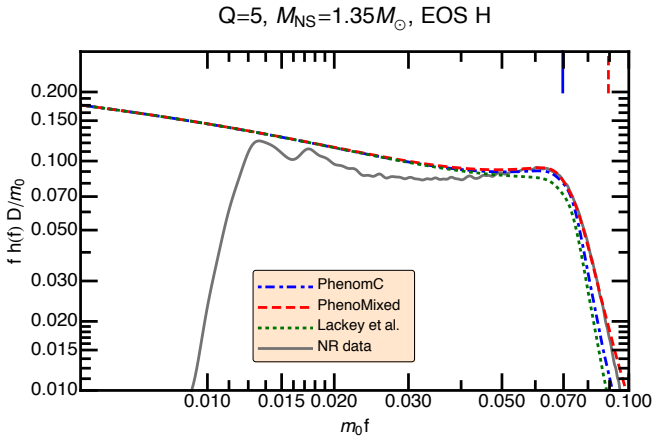

FIG. 2. BH-NS merger case `H-M135-Q5` (see Table I). The GW strain of the NR simulation (continuous grey) is compared to the BH-BH phenomenological model of [22] (dot-dashed blue), to the BH-NS model of [16] (dotted green), and to our BH-NS phenomenological model (dashed red). The location of the QNM frequency of the BH remnant is shown by the short, vertical, blue line in the top of the graph; the frequency at the onset of disruption frequency $m_0 f_{\rm tide}$ is indicated by the short, vertical, dashed, red line.

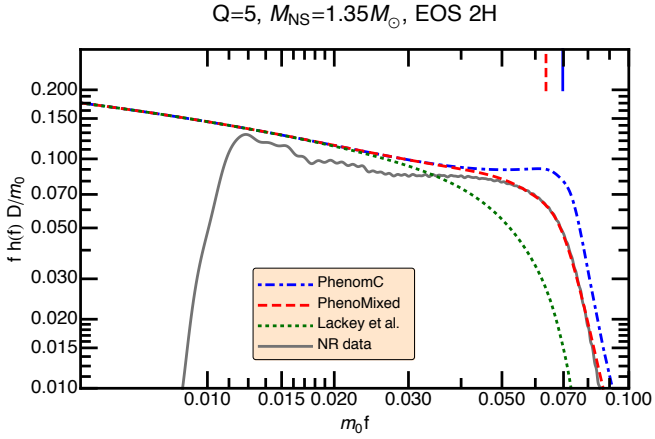

FIG. 3. BH-NS merger `2H-M135-Q5` (see Table I). In this plot (and in the remainder of this paper) we use the same color and linestyle conventions as in Fig. 2.

amplitude (see Appendix A). As mentioned previously, the deviation from the matching is then due to residual eccentricity in the numerical simulation and to the sudden onset of the GW emission: both features can be cured, the former numerically and the latter analytically, but addressing these aspects is beyond the scope of this paper. Setting $\tilde{f}_0 = \tilde{f}_{\rm RD} \equiv 0.99\times 0.98 f_{\rm RD}$ provides a better high-frequency matching than the BH-BH PhenomC prescription of using $0.98 f_{\rm RD}$. As anticipated, this small difference is not surprising, as the ringdown frequency is following from a different model for the properties of the BH remnant. This prescription for $\tilde{f}_0$ works for all nondisruptive coalescences. We set $\kappa = 1.25$ to achieve a better matching of the knee in the waveform spectrum. This same rescaling of γ_1 works for all other waveforms used to build our model. With the data currently available, the nature of this correction is unclear: it could be a "universal" correction, a consequence of residual eccentricity in the data, an artifact of trying to match GWs that are not the BH-BH hybrid ones with γ_1 values obtained from the BH-BH hybrid waveforms themselves, or it could have some other origin. It is reassuring, though, that the rescaling is unique. Perhaps longer, more accurate waveforms will lead to the conclusion that γ_1 should not be rescaled when passing from BH-BH to BH-NS mergers. We set $\sigma_{\rm tide} = 0$, $\epsilon_{\rm ins} = 1$, and $\epsilon_{\rm tide} = 1$, so that d (the shutoff frequency of the PN inspiral contribution) and δ_1 were not corrected: these values match our expectations, given the nondisruptive nature of this specific coalescence. Finally, the "fudge factor" correcting δ_2 was set to $\alpha = 1.35$.

B. Stiffening the EOS: tidal effects

In Fig. 2 we repeat the procedure for the $Q = 5$, $M_{\rm NS} = 1.35 M_\odot$, EOS H binary (`H-M135-Q5` in Table I). We set once again $\kappa = 1.25$ (note that this value of κ seems to always give a good match, independently of the EOS stiffness), $\epsilon_{\rm ins} = 1$, $\epsilon_{\rm tide} = 1$, $\sigma_{\rm tide} = 0$, $\alpha = 1.35$, and $\tilde{f}_0 = \tilde{f}_{\rm RD}$. The frequency at the onset of tidal disruption $f_{\rm tide}$, marked by the short, vertical, dotted red line, is now closer to $\tilde{f}_{\rm RD}$, marked by the short, vertical blue line. This means that the EOS stiffening gradually increases the relevance of tidal effects. The behavior of this merger, however, is still very BH-BH-like.

By further stiffening the EOS, we eventually hit a disruptive merger, for which $f_{\rm tide} < f_{\rm RD}$. This case is reported in Fig. 3, where we consider data from the run `2H-M135-Q5` in Table I. In this case, setting $\epsilon_{\rm ins} = 1$ and $\alpha = 1.35$, but $\epsilon_{\rm tide} = 0.49$, $\sigma_{\rm tide} = 0.041$, and $\tilde{f}_0 = f_{\rm tide}$ is required. As anticipated, $\sigma_{\rm tide}$ and $\epsilon_{\rm tide}$ need to be greater than 0 and smaller than 1, respectively, since this is a disruptive merger. This run shows that we must require the following prescription on the "windowing" frequency:

$$\tilde{f}_0 = \min[f_{\rm tide}, \tilde{f}_{\rm RD}]\,. \tag{27}$$

In the $\mathcal{C} \to 1/2$ limit, i.e. in the nonspinning BH-BH limit, $\tilde{f}_0 \equiv \tilde{f}_{\rm RD} = 0.99 \times 0.98 f_{\rm RD}$. This differs slightly from the $f_0 = 0.98 f_{\rm RD}$ used in [22]. The origin of this discrepancy is (again) in the different methods used to calculate the BH remnant parameters determining $f_{\rm RD}$.

Incidentally, the plots (and in particular Fig. 3) show that while the amplitude model developed by Lackey *et al.* [16] is accurate enough for BH-BH-like mergers, it becomes increasingly inaccurate when the NS EOS is particularly stiff (the same conclusion seems to hold in all other cases we have investigated). A possible origin of the discrepancy may be the fact that the model of Lackey and collaborators was calibrated also to the EOSs with $\Gamma_2 = 2.4$, 2.7, and 3.3 (15 altogether), in addition to the

6 $\Gamma_2 = 3.0$ EOSs, for a total of 21 EOSs. The 2H EOS is just one EOS out of 21 in this catalog. The price to pay for fitting more EOSs may thus be that results for the 2H EOS are less accurate.

Finally, we must understand the behavior of α, $\epsilon_{\rm ins}$, $\sigma_{\rm tide}$, and $\epsilon_{\rm tide}$. By trying to reproduce the GW spectra of all runs in Table I, we found that α depends on the binary mass ratio $Q = M_{\rm BH}/M_{\rm NS}$, or, equivalently, on the symmetric mass ratio $\nu = Q/(1+Q)^2$: cf. Fig. 4. Unfortunately, this dependence is poorly constrained, as our runs span values of Q from 2 to 5. We know, however, that our model for $\chi_{\rm f}$ (based on [47]) differs negligibly from the model for $\chi_{\rm f}$ used in [22] for $Q \geq 5$ (i.e. $\nu \leq 5/36$). We therefore decided to make the conservative choice of fitting our data in Fig. 4 with the function

$$\alpha = w^{-}_{\nu_0,d_0}(\nu) + 1 \tag{28}$$

for $\nu \geq 5/36$, while assuming α to be constant and equal to its value at $Q = 5$ (corresponding to $\nu = 5/36$) for $Q \geq 5$. This yields $\nu_0 = 0.146872$ and $d_0 = 0.0749456$.

In order to understand the behavior of $\epsilon_{\rm ins}$, $\sigma_{\rm tide}$, and $\epsilon_{\rm tide}$, we found it useful to divide the numerical runs in three groups (following the classification suggested in [52] for the outcome of a BH-NS coalescence):

- mergers with $f_{\rm tide} > \tilde{f}_{\rm RD}$ ("nondisruptive");
- mergers with $f_{\rm tide} < \tilde{f}_{\rm RD}$ and $M_{\rm b,torus} = 0$ ("mildly disruptive");
- mergers with $f_{\rm tide} < \tilde{f}_{\rm RD}$ and $M_{\rm b,torus} > 0$ ("strongly disruptive").

The first group shows a clear QNM excitation, the third group shows a sharp high-frequency cutoff of tidal origin, and the behavior of the second group is somewhere in between the other two. Out of the cases used to build our model (as listed in Table I) we have 6, 2, and 6 data sets for the first, second, and third group, respectively, so that the second group is not very populated. We expect to have more data (and to clarify the behavior of this second group) in the near future, when we will consider waveforms from merging binaries with nonzero initial spins.

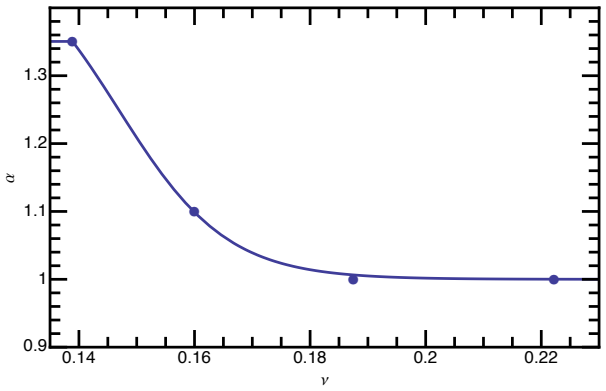

FIG. 4. Values of α (the factor correcting δ_2) versus ν. The fitting function is of the form $w^{-}_{\nu_0,d_0}(\nu)+1$, with $\nu_0 = 0.146872$ and $d_0 = 0.0749456$, for $\nu \geq 5/36$, i.e. for $Q \leq 5$. For $\nu < 5/36$ we assume α to be constant and equal to $w^{-}_{\nu_0,d_0}(5/36) + 1 \simeq 1.35$.

1. *Nondisruptive Mergers*

For nondisruptive mergers tidal effects are weak, the NS matter moves coherently and, thus, the merger and the inspiral contributions to the GW spectrum "fade out" at the same frequency: this implies that $\epsilon_{\rm ins} = 1$.

Let us now turn to $\epsilon_{\rm tide}$, the factor correcting δ_1 in Eq. (6). As shown in the top-left panel of Fig. 5, values of this parameter which allow our model to reproduce the spectra of the six nondisruptive mergers in Table I have a regular behavior if plotted as a function of the dimensionless quantity

$$x_{\rm ND} \equiv \left(\frac{f_{\rm tide} - \tilde{f}_{\rm RD}}{\tilde{f}_{\rm RD}}\right)^2 - 0.6\mathcal{C}\,. \tag{29}$$

This functional form captures the fact that a "large" NS suppresses ringdown excitation via destructive interference (cf. [53] for a toy model illustrating this phenomenon). The frequency at the onset of tidal disruption for a large NS is closer to the QNM frequency of the BH remnant. A fit of the form

$$\epsilon_{\rm tide} = 2w^{+}_{x_0,d_0}(x_{\rm ND}) \tag{30}$$

yields $x_0 = -0.0881657$ and $d_0 = 0.0661666$. The windowing function choice is motivated by observing that the ringdown amplitude is smoothly suppressed as tidal effects take over, i.e. as the NS disruption frequency approaches the QNM frequency of the BH remnant from above.

A similar approach is used for $\sigma_{\rm tide}$, which must vanish as the coalescence becomes more and more BH-BH-like. On the other hand, as tidal effects increase, $\sigma_{\rm tide}$ must grow and "smear" the signal shutoff. In this case, we fitted the six data points as follows:

$$\sigma_{\rm tide} = 2w^{-}_{x_0,d_0}(x_{\rm ND})\,, \tag{31}$$

obtaining $x_0 = -0.170321$ and $d_0 = 0.162074$. This fit is shown along with the data in the top-right panel of Fig. 5.

To summarize, for nondisruptive mergers we can set:

$$\epsilon_{\rm ins} = 1\,, \tag{32}$$

$$\epsilon_{\rm tide} = 2w^{+}_{x_0,d_0}(x_{\rm ND}) \quad \text{with} \quad \begin{cases} x_0 = -0.0881657 \\ d_0 = 0.0661666 \end{cases}, \tag{33}$$

$$\sigma_{\rm tide} = 2w^{-}_{x_0,d_0}(x_{\rm ND}) \quad \text{with} \quad \begin{cases} x_0 = -0.170321 \\ d_0 = 0.162074 \end{cases}. \tag{34}$$

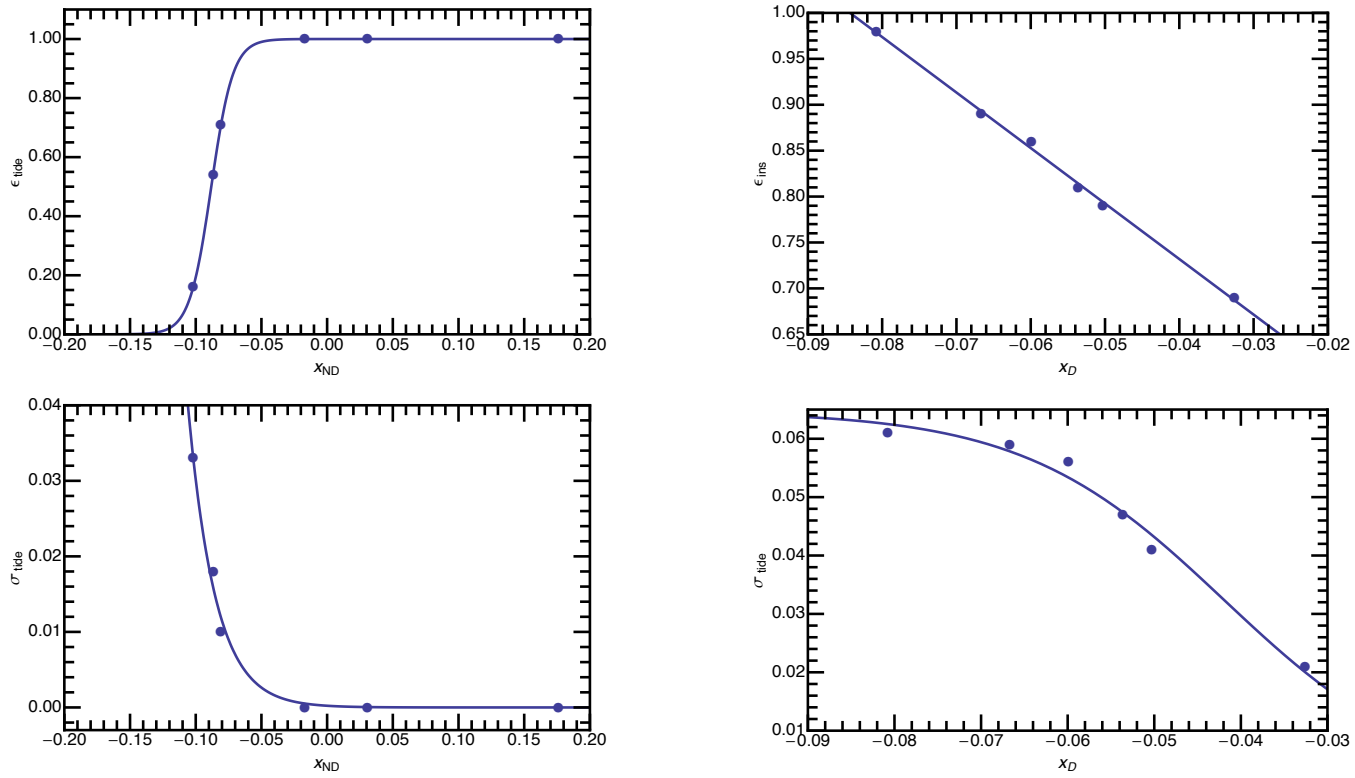

FIG. 5. Correction parameters appearing in our phenomenological models for nondisruptive mergers (left panels) and disruptive mergers (right panels). Top left: correction factor $\epsilon_{\rm tide}$ to δ_1 versus $x_{\rm ND}$, as defined in Eq. (29), for the six nondisruptive cases with $M_{\rm NS} = 1.35M_\odot$ and $\Gamma_2 = 3.0$. The data points are fitted by the function $2w^+_{x_0,d_0}(x_{\rm ND})$, with $x_0 = -0.088166$ and $d_0 = 0.066167$. Top right: correction factor $\epsilon_{\rm ins}$ to $\tilde{f}_0$ versus $x_{\rm D}$, as defined in Eq. (35), for the six disruptive cases with $M_{\rm NS} = 1.35M_\odot$ and $\Gamma_2 = 3.0$. The data points are fitted by the linear function $ax_{\rm D} + b$, with $a = -6.04599$ and $b = 0.490086$. Bottom left: the additive correction $\sigma_{\rm tide}$ to d versus $x_{\rm ND}$, as defined in Eq. (29), for the six nondisruptive cases with $M_{\rm NS} = 1.35M_\odot$ and $\Gamma_2 = 3.0$. The data points are fitted by the function $2w^-_{x_0,d_0}(x_{\rm ND})$, with $x_0 = -0.170321$ and $d_0 = 0.162074$. Bottom right: the additive correction $\sigma_{\rm tide}$ to d versus the $x_{\rm D}$, as defined in Eq. (35), for the six nondisruptive cases with $M_{\rm NS} = 1.35M_\odot$ and $\Gamma_2 = 3.0$. The data points are fitted by the function $Aw^-_{x_0,d_0}(x_{\rm D})$, with $x_0 = -0.0419235$, $d_0 = 0.0930419$, and $A = 0.129459$.

2. *Disruptive Mergers*

Tidal effects must be taken into account in the phenomenology of disruptive BH-NS mergers. The NS matter is scattered around and accretes onto the BH incoherently, no ringdown of the BH remnant is manifest in the GW spectrum, and therefore we have $\epsilon_{\rm tide} = 0$.

As tidal effects grow stronger, the PN inspiral description must be suppressed at smaller frequencies than the merger contribution. An effective description of the end of the merger contribution may be obtained by turning it off at $f_{\rm tide}$ [cf. Eq. (27)], so that $\epsilon_{\rm ins}\tilde{f}_0$ ends the inspiral contribution.

The values of $\epsilon_{\rm ins}$ that allow us to reproduce the spectra of the six disruptive mergers of Table I are well correlated with the following dimensionless quantity:

$$x_{\rm D} \equiv \frac{M_{\rm b,torus}}{M_{\rm b,NS}} + 2.23\mathcal{C} - 1.02\sqrt{\nu}. \tag{35}$$

A good linear fit to the data, as shown in the bottom-left panel of Fig. 5, is

$$\epsilon_{\rm ins} = 0.490086 - 6.04599x_{\rm D}\,. \tag{36}$$

The data for $\sigma_{\rm tide}$ also show a correlation with $x_{\rm D}$. A good fit is

$$\sigma_{\rm tide} = Aw^-_{x_0,d_0}(x_{\rm D}) \tag{37}$$

with $x_0 = -0.0419235$, $d_0 = 0.0930419$, and $A = 0.129459$. As shown in the bottom-right panel of Fig. 5, this fit is less robust than the previous ones, and our present model for $\sigma_{\rm tide}$ is quite likely to change as more data become available. However, in the rest of the paper we will show that this has a minor effect on the agreement between the BH-NS phenomenological waveforms and the numerical data.

To summarize, disruptive mergers are well reproduced

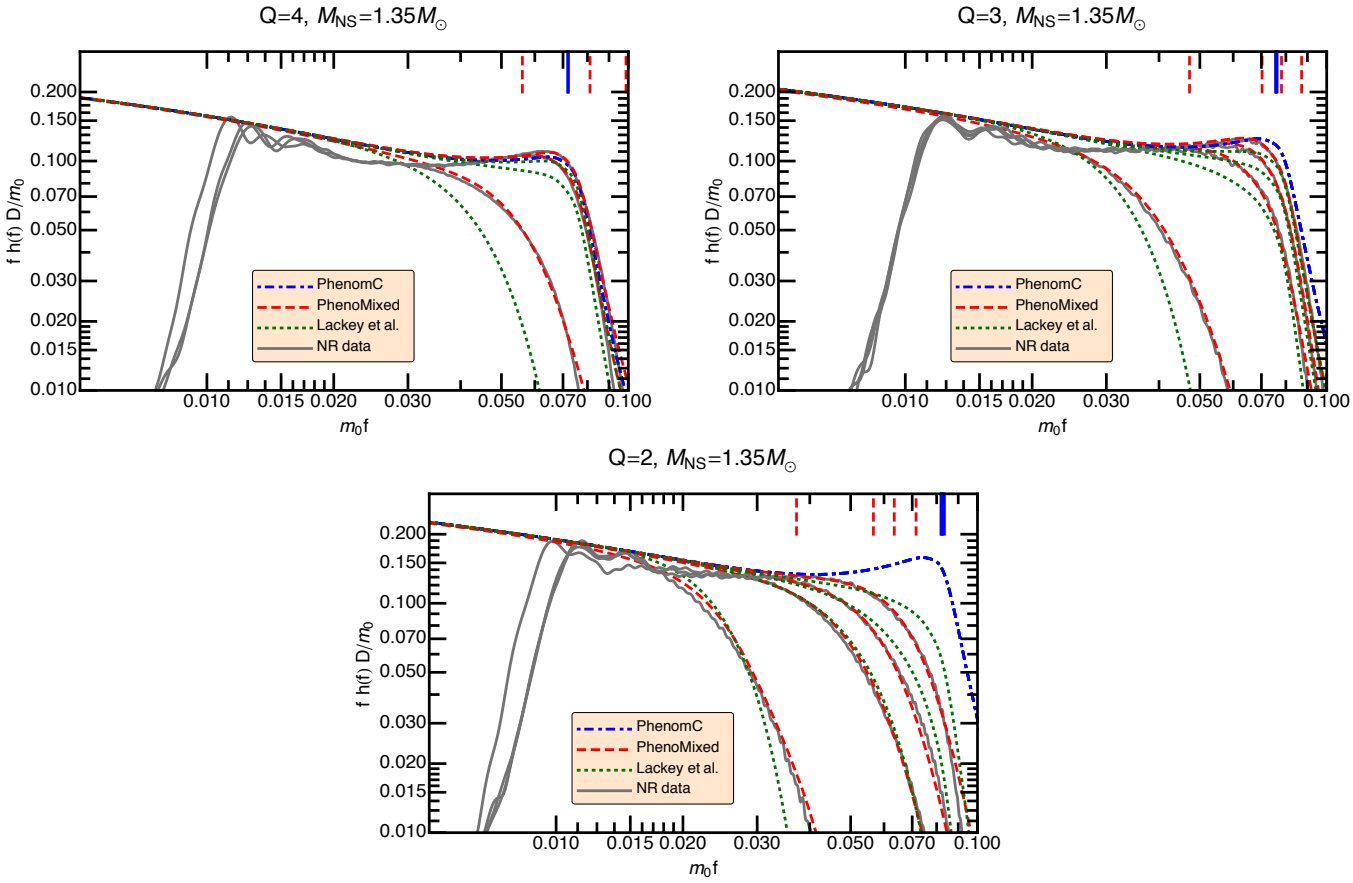

FIG. 6. The numerical simulations used to build the model (solid lines), discussed in Sec. V A, are compared to our phenomenological amplitude model (dashed lines), to the phenomenological amplitude model of Lackey *et al.* [16] (dotted lines) and to the BH-BH model of Santamaría *et al.* [22] (dash-dotted line). Top left: Cases `2H-M135-Q4`. `H-M135-Q4`, and `B-M135-Q4` (from left to right, so that the rightmost model is the closest to the BH-BH case). Top right: Cases `2H-M135-Q3`. `H-M135-Q3`, `HB-M135-Q3`, and `B-M135-Q3`. Bottom: Cases `2H-M135-Q2`, `H-M135-Q2`, `HB-M135-Q2`, and `B-M135-Q2`.

by setting

$$\epsilon_{\rm tide} = 0\,, \tag{38}$$

$$\epsilon_{\rm ins} = a x_{\rm D} + b \quad \text{with} \quad \begin{cases} a = -6.04599 \\ b = 0.490086 \end{cases}\,, \tag{39}$$

$$\sigma_{\rm tide} = A w^{-}_{x_0,d_0}(x_{\rm D}) \quad \text{with} \quad \begin{cases} A = 0.129459 \\ x_0 = -0.0419235 \\ d_0 = 0.0930419 \end{cases}\,. \tag{40}$$

3. *Mildly Disruptive Mergers*

Only two of the binaries in Table I have $M_{\rm b,torus} = 0$ and $f_{\rm tide} < \tilde{f}_{\rm RD}$, so that this regime is relatively poorly constrained by simulations. We expect the phenomenology in this case to be intermediate between the one of disruptive and nondisruptive mergers. In this sense it is reassuring to observe that:

1) $\epsilon_{\rm ins}$ may be determined as prescribed for disruptive mergers in Eq. (39), and
2) $\epsilon_{\rm tide}$ may be determined as prescribed for nondisruptive cases in Eq. (33).

These observations confirm that the nature of mildly disruptive coalescences is indeed somewhere in between the disruptive and nondisruptive cases. The value $\sigma_{\rm tide} = 0.041$ works for both mildly disruptive cases. We expect a better understanding of this class of mergers to emerge from future studies of BH-NS binaries with a spinning BH.

V. MODEL-DATA COMPARISONS

We may now see the model at work. In this section we collect and discuss the results for the GW spectra of all runs in Tables I and II. We follow the convention adopted in Figs. 1, 2, and 3 and show the numerical data with a grey, continuous line, the prediction of our model with a red, dashed line, the prediction of the PhenomC model with a blue, dot-dashed line, and the prediction of the BH-NS model of [16] with a green, dotted line. In ad-

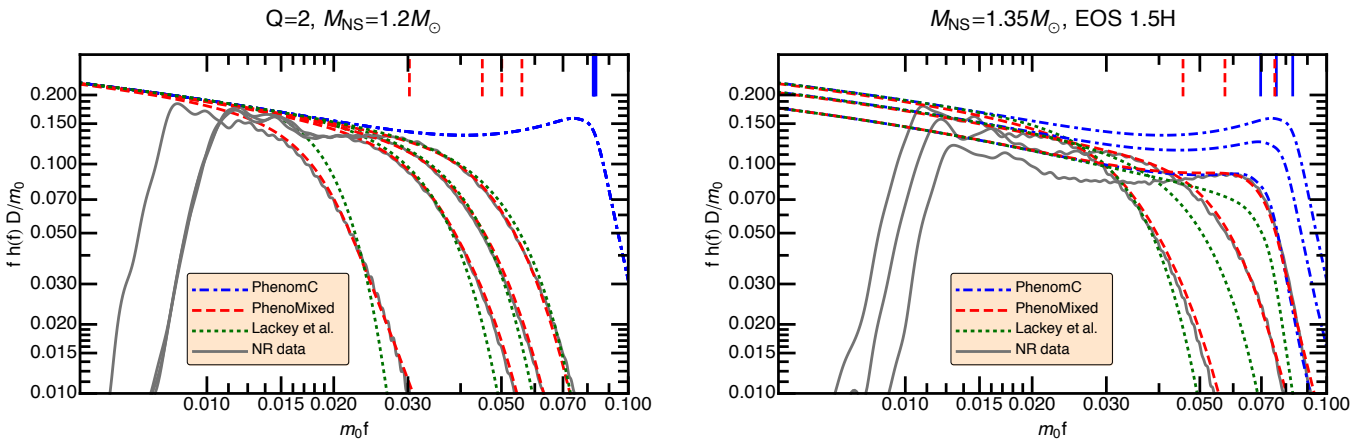

FIG. 7. Left: first set of numerical simulations used to test our model (cases `2H-M12-Q2`, `H-M12-Q2`, `HB-M12-Q2`, and `B-M12-Q2`), as discussed in Sec. V B. Right: second set of numerical simulations used to test our model (cases `1.5H-M135-Q2`, `1.5H-M135-Q3`, and `1.5H-M135-Q5`), as discussed in Sec. V C; we obtain similar results for the two remaining cases (not shown in this plot to avoid cluttering), i.e. `1.5H-M135-Q4` and `1.25H-M135-Q2`.

dition, the locations of the frequencies $\tilde{f}_{\rm RD}$ and $f_{\rm tide}$ are marked by short, vertical lines (straight blue and dashed red, respectively). We first show the remaining[2] GW spectra of the binaries in Table I, upon which our model is built. We then test our model against the binaries in Table II. We begin by looking at cases with $M \neq 1.35 M_\odot$, i.e. the four runs in the first block of Table II; we then consider the five cases in the second block of Table II, i.e. those with a $\Gamma_2 = 3.0$ core description, but that were not used when building the model; finally, we look at the fifteen binaries in which the NS core EOS has $\Gamma_2 \neq 3.0$.

A. The 14 Cases Used to Build the Model

In Figs. 1, 2, and 3 we showed how the model of Sec. II B, with hand-tuned parameters, performs for a subset of the binaries it was built upon, namely the three cases with mass ratio $Q = 5$. The variations in the GW spectra yielded by our model if we use the fits of the previous section for the parameters, instead of hand-tuned values, are negligible.

In Fig. 6 we illustrate the performance of our model for the three binaries with $Q = 4$, the four with $Q = 3$, and the four with $Q = 2$, respectively (see Table I). We apply the full procedure outlined in Sec. II B and explained in the previous section. Our model reproduces the high-frequency phenomenology very well, both for nondisruptive and disruptive mergers. In the case of disruptive mergers, in particular, when there is little or no QNM ringdown excitation of the BH remnant, we achieve a considerable improvement over the BH-BH phenomenological waveforms of [22] and also over the model by Lackey *et al.* [16]. Therefore our model should yield more accurate results for practical applications, including e.g. calculations of cutoff frequencies and SNRs. During the inspiral phase our model and the PhenomC model match, by construction, and we expect longer and more accurate numerical waveforms to better match the PN description of the inspiral GW amplitude, especially for mass ratios closer to unity, where the convergence of the PN expansion works best.

In conclusion, our model reproduces the high-frequency GW amplitude phenomenology for the fourteen runs upon which it was built. Furthermore, it performs much better than the BH-BH phenomenological waveform model and better than the model of [16], especially when mergers are disruptive.

B. The 4 Test Cases with $M_{\rm NS} \neq 1.35 M_\odot$

So far, we considered only binaries with $M_{\rm NS} = 1.35 M_\odot$. A first useful series of tests we can provide for our model thus involves binaries with a different NS mass. This may be done with the aid of our numerical data for four coalescences in which the NS has a mass of $1.2 M_\odot$ (first group of cases in Table II). We stress, once more, the fact that the data from these runs were *not* used to build the model.

The left panel of Figure 7 shows how our phenomenological model performs for these binaries. The tests are successful, in that (1) they correctly capture the phenomenology of all four mergers, and (2) they provide a more accurate description when compared to the PhenomC or Lackey *et al.* [16] amplitude models. It must be noted that all cases share the same, low mass ratio $Q = 2$, and that they are all disruptive mergers. In this sense, these tests may be viewed as being still limited, but the runs we have represent the current state of the

[2] Cases `B-M135-Q5`, `H-M135-Q5`, and `2H-M135-Q5` were already discussed in Sec. IV.

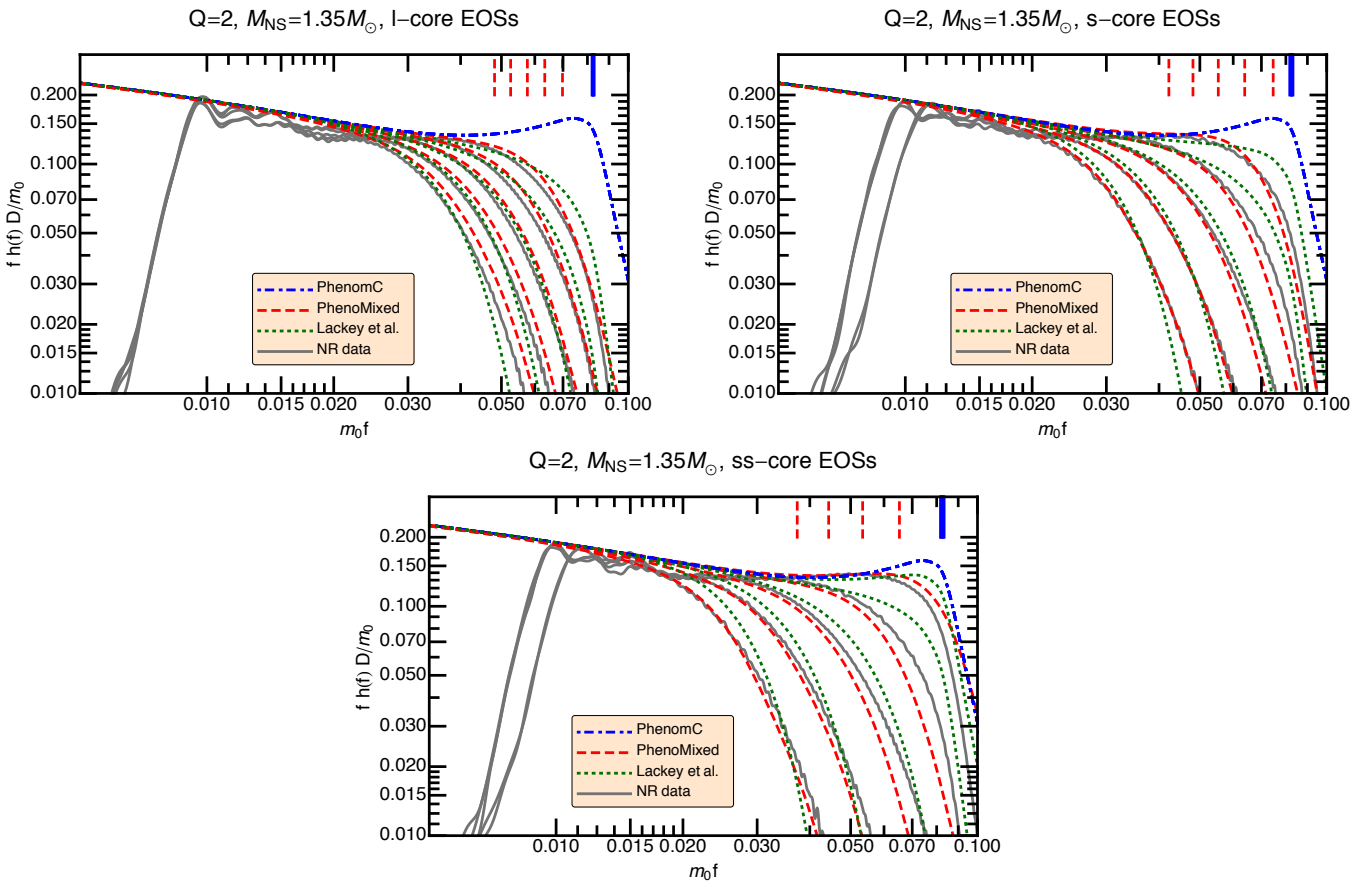

FIG. 8. Top left: cases `1.5Hl-M135-Q2`, `1.25Hl-M135-Q2`, `Hl-M135-Q2`, `HBl-M135-Q2`, and `Bl-M135-Q2`. Top right: cases `1.5Hs-M135-Q2`, `1.25Hs-M135-Q2`, `Hs-M135-Q2`, `HBs-M135-Q2`, and `Bs-M135-Q2`. Bottom: cases `1.5Hss-M135-Q2`, `1.25Hss-M135-Q2`, `Hss-M135-Q2`, `HBss-M135-Q2`, and `Bss-M135-Q2`.

art for nonspinning BH-NS mergers.

C. The 5 Test Cases with $\Gamma_2 = 3.0$

We now move to the second group of test cases in Table II. These five sets of data share a $\Gamma_2 = 3.0$ EOS description for the NS core and were not used when building the model. They are obtained by setting $\log P_{\rm fidu}$ to its value corresponding to the 1.5H or 1.25H EOS choices. Four data sets spanning different values of the binary mass ratio are available for the first choice, while a single data set for $Q = 2$ is available for the 1.25H EOS. Three of our results for the 1.5H EOS data are reported in the right panel of Fig. 7, where we demonstrate that these BH-NS merger typologies are correctly reproduced by our model. The remaining 1.5H EOS and the single 1.25H EOS datasets are reproduced with similar accuracy and are not shown to avoid cluttering in the plot. This ensures that our formulation is "universal" for data obtained with two-component piecewise polytropes having $\Gamma_2 = 3.0$ in the core.

D. The 15 Test Cases with $\Gamma_2 \neq 3$

The third and last set of BH-NS binary merger simulations in Table II is relative to NS models in which the core EOS description employs a polytropic exponent Γ_2 different from 3.0. All of these test cases are limited to mass ratio $Q = 2$. However, EOS-related effects on the binary dynamics, and hence on the GW phenomenology, are enhanced by low values of the binary mass ratio: with the exception of the astrophysically unlikely case of binaries with $Q < 2$, these data sets are therefore the most challenging possible test beds.

We present some results for the $\Gamma_2 \neq 3.0$ tests in the three panels of Fig. 8, which refer to $\Gamma_2 = 3.3$, $\Gamma_2 = 2.7$ and $\Gamma_2 = 2.4$, respectively (these are denoted as `l`, `s`, and `ss` in Table II). In each plot, we consider the results for the 1.5Hx, 1.25Hx, Hx, HBx, and Bx EOS, where x = {l, s, ss}. Overall, for cases with $\Gamma_2 = \{3.3, 2.7\}$ our model shows good agreement with the numerical data. An excellent match is evident for the `1.25Hl-M135-Q2` and for `1.5Hl-M135-Q2` data sets. With $\Gamma_2 = 2.4$, we run into our three worst test outcomes. These occur in the case of runs `Bss-M135-Q2`, `HBss-M135-Q2`, and `Hss-M135-Q2`, in order of decreasing agreement between

the numerical waveforms and our new phenomenological waveforms. Case `Bss-M135-Q2`, in particular, is a somewhat critical test. This happens because $f_{\rm RD} \simeq f_{\rm tide}$, which we know to be the hardest regime to model. For test cases `1.25Hss-M135-Q2` and `1.5Hss-M135-Q2`, on the other hand, we achieve a very good match between the model and the data.

The $\Gamma_2 = \{3.3, 2.7, 2.4\}$, $Q = 2$ test cases thus tell us that the model starts breaking down for systems in which the BH mass is low, and the NS is very compact and has an exceptionally soft core. This unfavorable region of the space of parameters is small, and probably astrophysically marginal, since current observations are gradually ruling out EOSs that predict a significant softening in the core [49, 50, 54]. Therefore our test pool provides a solid confirmation of the validity of our model.

VI. SIGNAL-TO-NOISE-RATIO COMPARISONS

In this Section we compare SNRs computed using our BH-NS amplitude model, the BH-BH PhenomC model of [22], and the restricted PN model used in several classic papers on GW data analysis [55, 56]. The SNR ρ for a frequency-domain signal $\tilde{h}(f)$ and a detector with noise power spectral density $S_h(f)$ is defined as

$$\rho \equiv 4\Re \int_{f_{\rm start}}^{f_{\rm end}} df \frac{\tilde{h}(f)\tilde{h}^*(f)}{S_h(f)} \,, \tag{41}$$

where $S_h(f)$ is the noise power spectral density of the detector, and $\tilde{h}(f)$ is defined in Eq. (A12) of Appendix A – i.e., it is a weighted average of the plus (+) and cross (×) polarization states. For any given binary system, we define the starting frequency $f_{\rm start}$ to be 10 Hz for second-generation detectors, and 1 Hz for third-generation detectors. Our convention on the ending frequency $f_{\rm end}$ will be discussed below.

In order to make our comparisons as "universal" as possible, we will consider *ratios* of SNRs, so that possible overall factors coming from distance, orientation, and inclination of the source cancel out. We define the following quantities, which are useful to understand the impact of modeling on detectability:

$$\epsilon_{\rm RPN} \equiv 1 - \frac{\rho_{\rm RPN}}{\rho_{\rm BHNS}} \,, \tag{42}$$

$$\epsilon_{\rm BHBH} \equiv 1 - \frac{\rho_{\rm BHBH}}{\rho_{\rm BHNS}} \,. \tag{43}$$

The first quantity ($\epsilon_{\rm RPN}$) measures the SNR deviation between a BH-NS waveform and a restricted PN (RPN) amplitude model — i.e., a zero-order amplitude expansion — obtained for the same masses of the binary constituents. Naturally, RPN waveforms (which are supposed to be accurate for inspirals only) deviate significantly from merger waveforms after the binary members cross the ISCO. Therefore, in order to provide a fair comparison, in this case we will follow much of the existing GW literature (e.g. [55, 56]) and truncate the SNR calculation at an upper frequency $f_{\rm end}$ that corresponds to the conventional Schwarzschild ISCO $r = 6m_0$ for a binary of total mass m_0.

The second quantity ($\epsilon_{\rm BHBH}$) measures the deviation between a BH-NS waveform amplitude model and the corresponding BH-BH waveform amplitude model for a nonspinning binary with the same masses. In this comparison[3] it makes sense to consider the whole waveform, and therefore we set $f_{\rm end} = 5000\,{\rm Hz}$ for all binaries.

We compute $\epsilon_{\rm RPN}$ and $\epsilon_{\rm BHBH}$ for all binaries in Tables I and II; in principle we could consider arbitrary binary configurations, but (to be conservative) here we limit our calculations to the cases for which we have evidence that our model works well.

We consider the following eight detectors: Advanced (Adv) LIGO, see e.g. Eq. (3.3) of [26]; Advanced LIGO in the zero-detuning, high-power configuration (AdvZDHP), as fitted in Eq. (4.7) of [57]; Advanced Virgo, Eq. (3.4) of [26]; the Einstein Telescope (ET) in broadband (B) and xylophone (C) configuration, as found in the MATLAB files available at [58]; and finally, KAGRA in the variable broadband (varBRSE), broadband optimized for NS-NS detection (maxBRSE), and variable detuned mode (varDRSE). We provide fits to the three KAGRA configurations in Appendix B (to our knowledge, no such fits have been published in the existing literature).

The results, collected in Table III, may be summarized as follows:

1) The deviations between the PhenomC model and our model increase as one considers binaries with stronger tidal effects. This is expected: the stronger the tidal effects, the larger the deviations between a BH-NS waveform and a BH-BH waveform with the same constituent masses. However, for the purpose of SNR calculations the PhenomC model and our model are basically equivalent: $|\epsilon_{\rm BHBH}| < 0.01$ for (nonspinning) BH-NS mergers. This is due to the fact that SNR calculations for these binaries are largely dominated by the low-frequency inspiral contribution. This result implies that using NR based BH-BH binary models in (say) rate calculations is good enough also for BH-NS binaries, at least in the nonspinning case.

2) The numbers listed for $|\epsilon_{\rm RPN}|$ show that NR-based modeling has an impact of at most $\sim 10\%$ in SNR calculations from BH-NS systems, as long as we truncate both signals at the Schwarzschild ISCO.

3) The deviations between different models are comparable for a given binary and different detectors (ET, KA-

[3] We also performed a similar comparison between our amplitude model and that of Lackey *et al.* [16], finding that $\epsilon_{\rm Lackey} \equiv 1 - \frac{\rho_{\rm Lackey}}{\rho_{\rm BHNS}} < 0.01$ in all cases. Therefore the waveform model of [16] is more than appropriate for SNR calculations in the case of nonspinning binaries.

TABLE III. $1-\rho_{\rm RPN}/\rho_{\rm BHNS}$ [in round brackets: $1-\rho_{\rm BHBH}/\rho_{\rm BHNS}$] for several detectors. $\rho_{\rm RPN}$ is the SNR calculated with the restricted PN model, while $\rho_{\rm BHNS}$ and $\rho_{\rm BHBH}$ are the SNRs obtained using our phenomenological BH-NS model and the PhenomC model. The numbers reported are percentages.

Run Label	LIGO		Virgo	KAGRA			ET	
	Adv	AdvZDHP	Adv	varBRSE	maxBRSE	varDRSE	B	C
EOSBQ5M135	−9.6 (0.0)	−6.5 (0.0)	−6.7 (0.0)	−7.0 (0.0)	−7.2 (0.0)	−8.1 (0.0)	−6.5 (0.0)	−4.8 (0.0)
EOSHQ5M135	−9.6 (0.0)	−6.5 (0.0)	−6.7 (0.0)	−7.0 (0.0)	−7.2 (0.0)	−8.1 (0.0)	−6.5 (0.0)	−4.8 (0.0)
EOS2HQ5M135	−9.6 (0.0)	−6.5 (0.0)	−6.7 (0.0)	−7.0 (0.0)	−7.2 (0.0)	−8.1 (0.0)	−6.5 (0.0)	−4.8 (0.0)
EOSBQ4M135	−7.8 (0.0)	−5.4 (0.0)	−5.8 (0.0)	−5.8 (0.0)	−5.9 (0.0)	−6.6 (0.0)	−5.3 (0.0)	−4.0 (0.0)
EOSHQ4M135	−7.8 (0.0)	−5.4 (0.0)	−5.8 (0.0)	−5.8 (0.0)	−5.9 (0.0)	−6.6 (0.0)	−5.3 (0.0)	−4.0 (0.0)
EOS2HQ4M135	−8.4 (−0.5)	−5.9 (−0.5)	−6.3 (−0.6)	−6.3 (−0.5)	−6.4 (−0.5)	−7.2 (−0.5)	−5.9 (−0.5)	−4.5 (−0.5)
EOSBQ3M135	−6.1 (0.0)	−4.3 (0.0)	−4.8 (0.0)	−4.6 (0.0)	−4.6 (0.0)	−5.2 (0.0)	−4.2 (0.0)	−3.2 (0.0)
EOSHBQ3M135	−6.1 (0.0)	−4.3 (0.0)	−4.8 (0.0)	−4.6 (0.0)	−4.6 (0.0)	−5.2 (0.0)	−4.2 (0.0)	−3.2 (0.0)
EOSHQ3M135	−6.1 (0.0)	−4.3 (0.0)	−4.8 (0.0)	−4.6 (0.0)	−4.6 (0.0)	−5.2 (0.0)	−4.2 (0.0)	−3.2 (0.0)
EOS2HQ3M135	−7.1 (−1.0)	−5.2 (−0.9)	−5.9 (−1.0)	−5.5 (−0.9)	−5.5 (−0.9)	−6.1 (−0.9)	−5.1 (−0.9)	−4.0 (−0.8)
EOSBQ2M135	−4.5 (−0.1)	−3.3 (−0.1)	−3.7 (−0.1)	−3.4 (−0.1)	−3.5 (−0.1)	−3.8 (−0.1)	−3.2 (−0.1)	−2.5 (−0.1)
EOSHBQ2M135	−4.6 (−0.2)	−3.4 (−0.2)	−3.9 (−0.2)	−3.5 (−0.2)	−3.6 (−0.2)	−4.0 (−0.2)	−3.3 (−0.2)	−2.6 (−0.2)
EOSHQ2M135	−4.8 (−0.4)	−3.5 (−0.4)	−4.0 (−0.4)	−3.7 (−0.3)	−3.7 (−0.3)	−4.1 (−0.4)	−3.4 (−0.3)	−2.7 (−0.3)
EOS2HQ2M135	−5.0 (−0.6)	−3.7 (−0.6)	−4.3 (−0.7)	−3.8 (−0.5)	−3.8 (−0.5)	−4.3 (−0.5)	−3.6 (−0.5)	−2.8 (−0.5)
EOSBQ2M12	−4.4 (−0.4)	−3.3 (−0.4)	−3.7 (−0.4)	−3.4 (−0.4)	−3.4 (−0.3)	−3.8 (−0.4)	−3.2 (−0.3)	−2.5 (−0.3)
EOSHBQ2M12	−4.5 (−0.5)	−3.4 (−0.5)	−3.8 (−0.5)	−3.5 (−0.4)	−3.5 (−0.4)	−3.9 (−0.5)	−3.2 (−0.4)	−2.6 (−0.4)
EOSHQ2M12	−4.5 (−0.5)	−3.4 (−0.5)	−3.9 (−0.5)	−3.5 (−0.5)	−3.5 (−0.5)	−3.9 (−0.5)	−3.3 (−0.5)	−2.6 (−0.4)
EOS2HQ2M12	−4.7 (−0.6)	−3.6 (−0.7)	−4.3 (−0.9)	−3.6 (−0.6)	−3.6 (−0.5)	−4.0 (−0.6)	−3.4 (−0.5)	−2.7 (−0.5)
EOS15HQ5M135	−9.6 (0.0)	−6.5 (0.0)	−6.7 (0.0)	−7.0 (0.0)	−7.2 (0.0)	−8.1 (0.0)	−6.5 (0.0)	−4.8 (0.0)
EOS15HQ4M135	−7.8 (0.0)	−5.4 (0.0)	−5.8 (0.0)	−5.8 (0.0)	−5.9 (0.0)	−6.6 (0.0)	−5.4 (0.0)	−4.1 (0.0)
EOS15HQ3M135	−6.6 (−0.5)	−4.8 (−0.5)	−5.3 (−0.5)	−5.0 (−0.5)	−5.1 (−0.5)	−5.7 (−0.5)	−4.7 (−0.4)	−3.7 (−0.4)
EOS125HQ2M135	−4.9 (−0.5)	−3.6 (−0.5)	−4.1 (−0.5)	−3.8 (−0.4)	−3.8 (−0.4)	−4.2 (−0.5)	−3.5 (−0.4)	−2.8 (−0.4)
EOS15HQ2M135	−4.9 (−0.5)	−3.7 (−0.5)	−4.2 (−0.6)	−3.8 (−0.5)	−3.8 (−0.5)	−4.3 (−0.5)	−3.6 (−0.5)	−2.8 (−0.5)
EOSBlQ2M135	−4.5 (−0.1)	−3.3 (−0.1)	−3.8 (−0.1)	−3.4 (−0.1)	−3.5 (−0.1)	−3.9 (−0.1)	−3.2 (−0.1)	−2.5 (−0.1)
EOSHBlQ2M135	−4.6 (−0.2)	−3.4 (−0.2)	−3.9 (−0.2)	−3.5 (−0.2)	−3.6 (−0.2)	−4.0 (−0.2)	−3.3 (−0.2)	−2.6 (−0.2)
EOSHlQ2M135	−4.7 (−0.4)	−3.5 (−0.3)	−4.0 (−0.4)	−3.7 (−0.3)	−3.7 (−0.3)	−4.1 (−0.3)	−3.4 (−0.3)	−2.7 (−0.3)
EOS125HlQ2M135	−4.9 (−0.5)	−3.6 (−0.4)	−4.1 (−0.5)	−3.8 (−0.4)	−3.8 (−0.4)	−4.2 (−0.4)	−3.5 (−0.4)	−2.8 (−0.4)
EOS15HlQ2M135	−4.9 (−0.5)	−3.7 (−0.5)	−4.2 (−0.5)	−3.8 (−0.5)	−3.8 (−0.5)	−4.2 (−0.5)	−3.5 (−0.5)	−2.8 (−0.4)
EOSBsQ2M135	−4.4 (0.0)	−3.2 (0.0)	−3.6 (0.0)	−3.3 (0.0)	−3.3 (0.0)	−3.7 (0.0)	−3.1 (0.0)	−2.4 (0.0)
EOSHBsQ2M135	−4.6 (−0.2)	−3.4 (−0.2)	−3.9 (−0.2)	−3.5 (−0.2)	−3.6 (−0.2)	−4.0 (−0.2)	−3.3 (−0.2)	−2.6 (−0.2)
EOSHsQ2M135	−4.8 (−0.4)	−3.6 (−0.4)	−4.0 (−0.4)	−3.7 (−0.4)	−3.7 (−0.4)	−4.1 (−0.4)	−3.4 (−0.4)	−2.7 (−0.4)
EOS125HsQ2M135	−4.9 (−0.5)	−3.7 (−0.5)	−4.2 (−0.5)	−3.8 (−0.5)	−3.8 (−0.5)	−4.2 (−0.5)	−3.5 (−0.5)	−2.8 (−0.4)
EOS15HsQ2M135	−5.0 (−0.6)	−3.7 (−0.6)	−4.3 (−0.6)	−3.8 (−0.5)	−3.9 (−0.5)	−4.3 (−0.5)	−3.6 (−0.5)	−2.8 (−0.5)
EOSBssQ2M135	−4.4 (0.0)	−3.2 (0.0)	−3.7 (0.0)	−3.3 (0.0)	−3.4 (0.0)	−3.8 (0.0)	−3.1 (0.0)	−2.4 (0.0)
EOSHBssQ2M135	−4.6 (−0.2)	−3.4 (−0.2)	−3.8 (−0.2)	−3.5 (−0.2)	−3.5 (−0.2)	−3.9 (−0.2)	−3.3 (−0.2)	−2.6 (−0.2)
EOSHssQ2M135	−4.8 (−0.6)	−3.6 (−0.6)	−4.1 (−0.7)	−3.7 (−0.5)	−3.8 (−0.5)	−4.2 (−0.5)	−3.5 (−0.5)	−2.8 (−0.5)
EOS125HssQ2M135	−5.0 (−0.4)	−3.7 (−0.4)	−4.2 (−0.4)	−3.8 (−0.4)	−3.9 (−0.4)	−4.3 (−0.4)	−3.6 (−0.4)	−2.8 (−0.4)
EOS15HssQ2M135	−5.0 (−0.6)	−3.7 (−0.5)	−4.3 (−0.6)	−3.8 (−0.5)	−3.8 (−0.5)	−4.3 (−0.5)	−3.6 (−0.5)	−2.8 (−0.5)

GRA and Advanced LIGO/Virgo). Among the three configurations of KAGRA, the variable configuration in broadband mode systematically yields the smallest deviations (in absolute value). Among second-generation detectors, SNR calculations for Advanced LIGO are the most sensitive to the high-frequency behavior of BH-NS merger waveforms.

VII. CUTOFF FREQUENCIES

The amplitude of the GWs emitted by a coalescing compact binary dies off at high frequency, once the newly formed object (be it a BH or a NS) settles down to a stationary equilibrium configuration. In the case of BH binaries, the GW amplitude drops at the frequency of the dominant ($l = m = 2$, $n = 0$) QNM mode of the remnant BH. In the case of BH-NS binaries, the cutoff, or shut down, frequency has received much attention because, depending on the dynamical history of the system, this frequency may originate from the tidal disruption of the NS. A cutoff frequency in the GW amplitude of BH-NS binaries that is due to the tidal disruption of the NS by the BH is dependent on the NS EOS. This has suggested the idea of examining the cutoff frequency of GWs emitted by mixed binaries in order to pin down the NS EOS (see e.g. [59–61]).

The first studies of cutoff frequencies, $f_{\rm Cut}$, for BH-NS binaries involved either semi-analytical [59–61] or fully numerical [62] (quasi-)equilibrium approaches. More recent estimates of $f_{\rm Cut}$ were determined via fully-relativistic numerical simulations of BH-NS mergers [41, 52, 63]. In these cases, $f_{\rm Cut}$ was defined to be a parameter obtained from analytical fits of the numerical GW data. This definition has the drawback of being viable only if numerical data are available for the binary of interest. Furthermore, the form of the fit to the GW data (and therefore the definition of the cutoff frequency) had to be revised when nonzero BH spins were considered.

In order to overcome these drawbacks, here we introduce a general definition of $f_{\rm Cut}$ that is of immediate application to any BH-NS GW spectrum, be it analytical or numerical. Our definition allows for a straightforward comparison among GW spectra originating from different models and/or calculations for the same binary, and for consistent comparisons among binaries with different physical parameters. The expression of the GW amplitude $\tilde{A}_{\rm Phen}(f)$ in Eq. (25) shows that at low frequencies, during the inspiral stage, $\tilde{A}_{\rm Phen}(m_0 f) \sim (m_0 f)^{-7/6}$. At high frequencies, instead, we have $\tilde{A}_{\rm Phen}(m_0 f) \sim (m_0 f)^{-19/6}$. Furthermore (and as already noted in [22] for the BH-BH case), the numerical data for BH-NS binaries show a high-frequency falloff that is faster than $(m_0 f)^{-19/6}$: for example, in [52] this falloff was fitted by a function of the form $e^{-(f/f_0)^\sigma}/f$, where f_0 and σ are two positive, real parameters. These considerations on the low- and high-frequency behavior imply that $(m_0 f)^2 \tilde{h}(m_0 f)$ must have a global maximum. Therefore we first look for the frequency $f_{\rm Max}$ such that $(m_0 f)^2 \tilde{h}(m_0 f)$ has a maximum, and then we define $f_{\rm Cut}$ to be the frequency (greater than $f_{\rm Max}$) at which

$$e m_0 f_{\rm Cut} \tilde{h}(m_0 f_{\rm Cut}) = m_0 f_{\rm Max} \tilde{h}(m_0 f_{\rm Max})\,. \qquad (44)$$

This definition of the cutoff frequency is independent of the details of the waveform, and it works for any $\tilde{h}(f)$ (given in either analytical or numerical form). We would once more like to draw the reader's attention to the conversion formula between dimensionless frequencies of the form $m_0 f$ and frequencies in Hz, which is given in Eq. (26).

Using our phenomenological model and the definition above, we computed contour plots of the cutoff frequency in the ($M_{\rm NS}$, $M_{\rm BH}/M_{\rm NS}$) plane. The results are shown in Fig. 9, where each panel refers to a different piecewise polytropic EOS (B, HB, H, 2H). The two white lines in each panel divide the plane in three regions, following the classification discussed in Section IV B.

In the top-right region the BH-NS coalescence is nondisruptive. This region is by far the largest for the soft EOS B (i.e., when the NS structure does not matter much) and it shrinks as we consider stiffer and stiffer EOSs. The cutoff frequency in this region is essentially the fundamental QNM of the remnant BH. In the bottom-left region the merger is disruptive, and mildly disruptive coalescences occur in the region comprised between the two white lines. This plot confirms the conclusion of previous studies (e.g. [64]), i.e. that the information from tidal disruptions is confined to high frequencies, where second-generation detectors will not be very sensitive for hypothetically typical events at a distance of 100Mpc or more: even for the stiffest EOS 2H, the observation of EOS effects will require third-generation detectors such as ET, that are sensitive at frequencies $\gtrsim 1\,$kHz.

What is most interesting (in our view) is that the calculations presented in Fig. 9 could provide a basis to address the inverse problem: given future observations of a tidal disruption frequency, what can we say about the EOS prevailing in the interior? We will address this question after working out a generalization of the present calculations to the case of spinning BH-NS mergers.

VIII. CONCLUSIONS

In this paper we developed a phenomenological model for the frequency-domain gravitational waveform amplitude of nonspinning BH-NS mergers. The model was calibrated to general relativistic numerical simulations using a piecewise polytropic neutron star EOS with a $\Gamma_2 = 3.0$ core, and it encompasses the three possible outcomes of the merger: no tidal disruption, "mild", and "strong" tidal disruption. We showed that the model is very accurate even in the most challenging cases, namely when the core EOS has a very small polytropic exponent and the binary mass ratio is small ($\Gamma_2 = 2.4$ and $Q = 2$), so

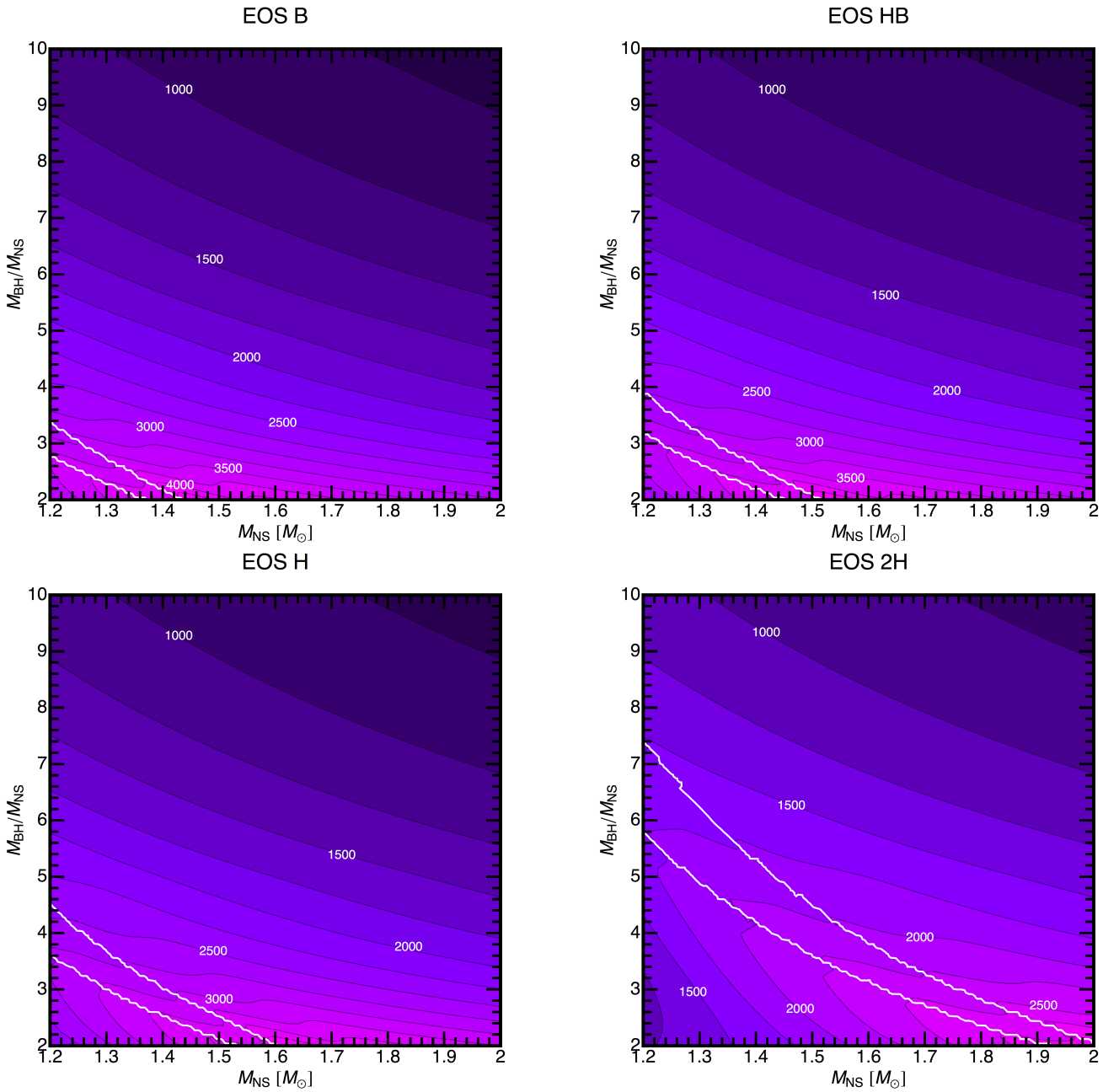

FIG. 9. The cutoff frequency $f_{\rm Cut}$, as defined in Eq. (44), computed with our BH-NS GW amplitude model. We consider the EOSs B, HB, H, 2H, and report contour lines in Hz, with a spacing of 250 Hz. The two white lines in each panel divide the plane in three regions: a top-right one in which the BH-NS coalescences are nondisruptive, a bottom-left one in which they are disruptive, and a middle region in which mildly disruptive coalescences occur. This classification is discussed in Section IV B.

that the frequency at the onset of tidal disruption and the ringdown frequency of the final BH are very close to each other ($f_{\rm RD} \simeq f_{\rm tide}$). A *Mathematica* notebook implementing the algorithm is publicly available online [65].

We demonstrated that such an accurate modeling of the waveform amplitude is probably unnecessary for SNR calculations and rate estimates from nonspinning BH-NS binaries (cf. [8, 9]), in the sense that BH-BH phenomenological waveforms provide SNRs accurate within about a percent for second- and third-generation GW interferometers. This may not be true for mergers of *spinning* BH-NS binaries: by comparing SNRs for GWs obtained with the PhenomC model of [22] and with the model of [16], we found differences up to $\sim 10\%$. The most immediate (and probably the most useful) application of the model will be to extract information on the nuclear EOS from future high-frequency GW observations, using

e.g. the high-frequency signal cutoff frequencies that we provided in Fig. 9 (see [59–61] for previous studies in this direction).

In the near future we plan to extend and improve the model as longer and more accurate numerical waveforms become available. In particular, we will improve the model in the underconstrained mild tidal disruption regime, extend it to aligned, spinning binaries [16, 52], and possibly also to precessing/inclined binaries [66, 67]. Future work should also address the development of a similar phenomenological model for the waveform phasing, the extension to higher multipoles of the radiation (beyond $l = m = 2$), and possibly comparisons with the EOB formalism. All of these extensions will rely critically on the accuracy of available numerical simulations (see [34, 68] for a discussion in the context of NS-NS binaries).

Acknowledgements. This work was supported in part by the DFG grant SFB/Transregio 7. E.B. is supported by NSF CAREER Grant No. PHY-1055103. K.K. is supported by a JSPS Postdoctoral Fellowship for Research Abroad. We are grateful to Masaki Ando for helpful correspondence on the KAGRA power spectral density. F.P. wishes to thank Frank Ohme for useful discussions on the PhenomC model, and Luciano Rezzolla for reading the manuscript. This work was supported by the Japanese Grant-in-Aid for Scientific Research (21340051, 24740163), and by the Grant-in-Aid for Scientific Research on Innovative Area (20105004). Part of this work was completed during a long-term workshop on Gravitational Waves and Numerical Relativity held at the Yukawa Institute for Theoretical Physics of Kyoto University in 2013.

Appendix A: Matching Numerical and Analytical Amplitudes

When building our amplitude model [Eq. (25)], the first thing to do is to ensure that the same convention is used for the overall amplitude of the numerical gravitational waveform data and in Eq. (1) for the BH-BH PhenomC GWs of [22], that are our starting point.

We begin by writing out the plus and cross polarization of the quadrupole moment of the emitted gravitational radiation. This are

$$h_+ = \frac{1}{2}\left[h_{22}({}_{-2}Y^{22} + {}_{-2}Y^{2-2*}) + h^*_{22}({}_{-2}Y^{22*} + {}_{-2}Y^{2-2})\right] , \tag{A1}$$

$$h_\times = \frac{i}{2}\left[h_{22}({}_{-2}Y^{22} - {}_{-2}Y^{2-2*}) + h^*_{22}({}_{-2}Y^{2-2} - {}_{-2}Y^{2-2})\right] , \tag{A2}$$

where the ${}_{-s}Y^{lm}$'s denote spin-weighted spherical harmonics. If we pick an optimal observer, that is if we place the observer "face-on" by setting the angles $\theta = 0$ and $\phi = 0$ with respect to the source, the harmonics become

$${}_{-2}Y^{22} = \sqrt{\frac{5}{4\pi}} , \tag{A3}$$

$${}_{-2}Y^{2-2} = 0 , \tag{A4}$$

and reduce the expressions for the two GW polarizations to

$$h_+ = \frac{1}{2}\sqrt{\frac{5}{4\pi}}\left(h_{22} + h^*_{22}\right) , \tag{A5}$$

$$h_\times = \frac{i}{2}\sqrt{\frac{5}{4\pi}}\left(h_{22} - h^*_{22}\right) . \tag{A6}$$

These are the quantities we obtain from our numerical simulations. We may also express $h_{+,\times}$ using the amplitude A_{22} and the phase Φ of $h_{22} = A_{22}e^{2i\Phi}$. This yields

$$h_+(t) = \sqrt{\frac{5}{4\pi}}|A_{22}(t)|\cos\Phi(t) , \tag{A7}$$

$$h_\times(t) = \sqrt{\frac{5}{4\pi}}|A_{22}(t)|\sin\Phi(t) , \tag{A8}$$

where we explicitly wrote out the time dependence.

When transforming to the Fourier domain in the stationary phase approximation[4], special attention must be paid:

$$\tilde{h}_+(f) = \sqrt{\frac{5}{4\pi}}\frac{|A_{22}(t_{\rm f})|}{2}\sqrt{\frac{\pi}{\dot{\omega}}}e^{i\Psi(f)} , \tag{A9}$$

$$\tilde{h}_\times(f) = \sqrt{\frac{5}{4\pi}}\frac{|A_{22}(t_{\rm f})|}{2}\sqrt{\frac{\pi}{\dot{\omega}}}e^{i\Psi(f)} , \tag{A10}$$

where ψ is the Fourier phase, and where $t_{\rm f}$ is the moment of time when the instantaneous frequency coincides with the Fourier variable, i.e., $M\omega(t_{\rm f}) = 2\pi f$, ω being the time derivative of $\Phi(t)$. Notice the $1/2$ factor that appears in these expressions. If one instead transforms directly $h_{22}(t) = A_{22}(t)e^{2i\Phi(t)}$, as is done in [22], one gets

$$\tilde{h}_{22}(f) = |A_{22}(t_{\rm f})|\sqrt{\frac{\pi}{\dot{\omega}}}e^{i\Psi(f)} . \tag{A11}$$

We then consider the GW strain

$$\sqrt{\frac{|\tilde{h}_+|^2 + |\tilde{h}_\times|^2}{2}} , \tag{A12}$$

which is the quantity calculate from our numerical data and plotted throughout the paper. By using the previous equalities we see that

$$\sqrt{\frac{|\tilde{h}_+|^2 + |\tilde{h}_\times|^2}{2}} = \frac{1}{2}\sqrt{\frac{5}{4\pi}}|A_{22}(t_{\rm f})|\sqrt{\frac{\pi}{\dot{\omega}}} = \frac{1}{2}\sqrt{\frac{5}{4\pi}}|\tilde{h}_{22}| \tag{A13}$$

[4] This is done to obtain the $\tilde{A}_{\rm PN}$ terms of Eq. (1) used in [22] and here.

This shows that the factor

$$\frac{1}{2}\sqrt{\frac{5}{4\pi}} \tag{A14}$$

must be used to translate between the PN frequency-domain expression of [22] and the amplitude seen by an observer in the direction of the rotational axis of the binary.

Appendix B: KAGRA Sensitivity Curve Fits

In this appendix we provide analytical fits to the estimated sensitivity limits of KAGRA, available at the KAGRA webpage [3]. We consider three different configurations. In the first case, we fit the total noise data for the KAGRA variable configuration in broadband mode (varBRSE); in the second case, we look at the total noise curve of KAGRA in the broadband mode, optimized for BNS inspiral detection without detuning (maxBRSE); in the third and last case, we examine the variable KAGRA configuration in detuned mode (varDRSE).

The total noise data for the three KAGRA configurations may be fitted with the following curve:

$$S_h(f) = s_0 \left(a_2 \bar{f}^2 + a_1 \bar{f} + 1 + \right. \tag{B1}$$
$$\left. + \frac{b_{05}}{\sqrt{\bar{f}}} + \frac{b_1}{\bar{f}} + \frac{b_2}{\bar{f}^2} + \frac{b_3}{\bar{f}^3} + \frac{b_4}{\bar{f}^4} + \frac{b_5}{\bar{f}^5} + \frac{b_{16}}{\bar{f}^{16}}\right) ,$$

where $\bar{f} = f/f_0$, f_0 being the frequency location of the minimum of the quantum noise in the configuration one is considering. This is 84.3335 Hz in broadband mode, i.e. for varBRSE and maxBRSE, and 83.3681 Hz in detuned mode, that is, for varDRSE. The form of this fit follows automatically when considering the individual contributions to the total noise and adding them up. There are two power laws for the mirror noise, one for the seismic noise, one for the suspension noise, and seven for the total quantum noise. The mirror noise and the total quantum noise share a $\sim 1/f$ term so that there is a total of ten power laws and, hence, of ten parameters to be fitted. The results of the fits are collected in Table IV for the three KAGRA configurations varBRSE, maxBRSE, and varDRSE, and are shown in the three panels of Figure 10, along with the original data.

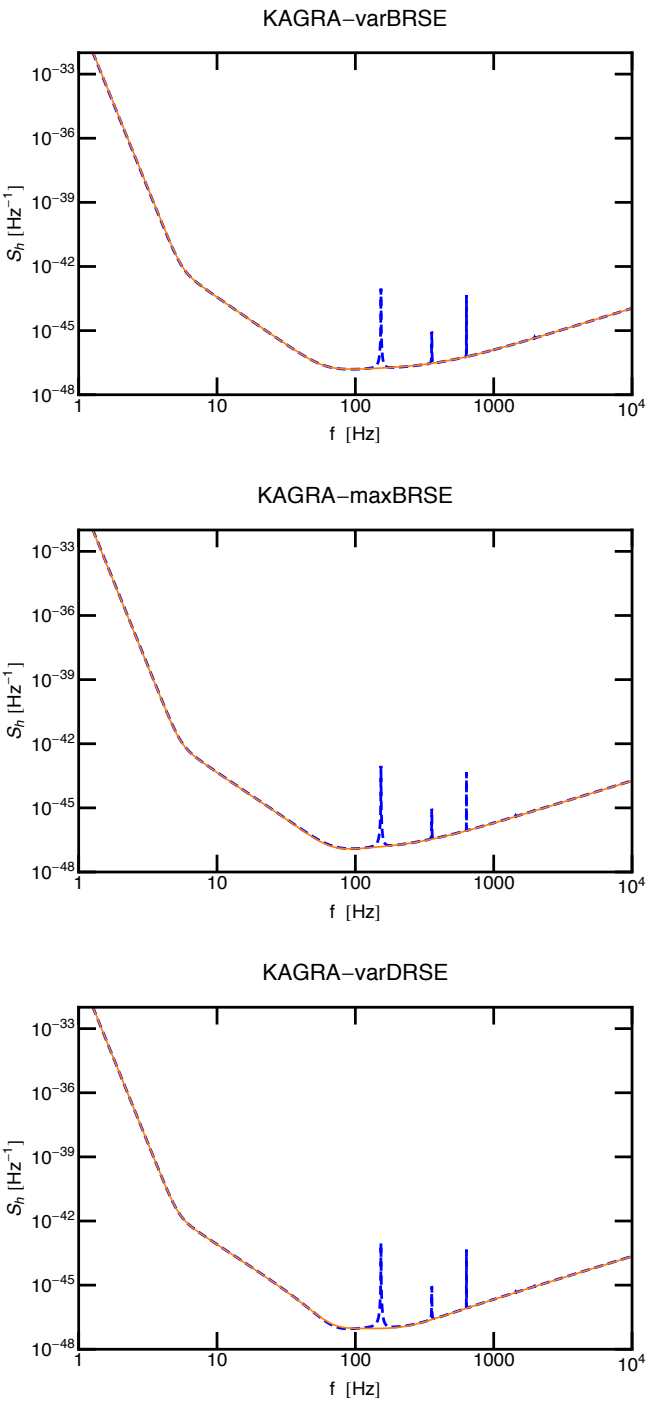

FIG. 10. Total noise data for KAGRA (dashed blue) and its best fit (continuous orange). The top panel refers to the variable KAGRA configuration in broadband mode (varBRSE); the middle panel refers to KAGRA in broadband mode and optimized for BNS inspiral detection (maxBRSE); the bottom panel refers to the variable KAGRA configuration in detuned mode (varDRSE).

[1] G. M. Harry and the LIGO Scientific Collaboration, Class. Quantum Grav. **27**, 084006 (2010).
[2] K. Somiya (KAGRA Collaboration), Class.Quant.Grav. **29**, 124007 (2012), arXiv:1111.7185 [gr-qc].
[3] KAGRA webpage, `http://gwcenter.icrr.u-tokyo.ac.jp/en/researcher/parameter` (2013).
[4] IndIGO webpage, `http://www.gw-indigo.org/` (2012).
[5] M. Punturo *et al.*, Class. Quantum Grav. **27**, 194002 (2010).
[6] B. Aylott, J. G. Baker, W. D. Boggs, M. Boyle, P. R. Brady, *et al.*, Class.Quant.Grav. **26**, 165008 (2009), arXiv:0901.4399 [gr-qc].
[7] P. Ajith, M. Boyle, D. A. Brown, B. Brugmann, L. T. Buchman, *et al.*, Class.Quant.Grav. **29**, 124001 (2012), arXiv:1201.5319 [gr-qc].
[8] J. Abadie *et al.* (LIGO Scientific Collaboration, Virgo Collaboration), Class.Quant.Grav. **27**, 173001 (2010), arXiv:1003.2480 [astro-ph.HE].
[9] M. Dominik, K. Belczynski, C. Fryer, D. Holz, E. Berti, *et al.*, Astrophys.J. **759**, 52 (2012), arXiv:1202.4901 [astro-ph.HE].
[10] S. Marassi, R. Schneider, G. Corvino, V. Ferrari, and S. Portegies Zwart, Phys.Rev. **D84**, 124037 (2011), arXiv:1111.6125 [astro-ph.CO].
[11] X.-J. Zhu, E. J. Howell, D. G. Blair, and Z.-H. Zhu, (2012), arXiv:1209.0595 [gr-qc].
[12] J. S. Read, C. Markakis, M. Shibata, K. Uryu, J. D. Creighton, *et al.*, Phys.Rev. **D79**, 124033 (2009), arXiv:0901.3258 [gr-qc].
[13] J. S. Read, L. Baiotti, J. D. E. Creighton, J. L. Friedman, B. Giacomazzo, *et al.*, (2013), arXiv:1306.4065 [gr-qc].
[14] A. Bauswein, H.-T. Janka, K. Hebeler, and A. Schwenk, Phys. Rev. D **86**, 063001 (2012), arXiv:1204.1888 [astro-ph.SR].
[15] B. D. Lackey, K. Kyutoku, M. Shibata, P. R. Brady, and J. L. Friedman, Phys.Rev. **D85**, 044061 (2012), arXiv:1109.3402 [astro-ph.HE].
[16] B. D. Lackey, K. Kyutoku, M. Shibata, P. R. Brady, and J. L. Friedman, (2013), arXiv:1303.6298 [gr-qc].
[17] P. Ajith, S. Babak, Y. Chen, M. Hewitson, B. Krishnan, *et al.*, Class.Quant.Grav. **24**, S689 (2007), arXiv:0704.3764 [gr-qc].
[18] P. Ajith, S. Babak, Y. Chen, M. Hewitson, B. Krishnan, *et al.*, Phys.Rev. **D77**, 104017 (2008), arXiv:0710.2335 [gr-qc].
[19] P. Ajith, Class.Quant.Grav. **25**, 114033 (2008), arXiv:0712.0343 [gr-qc].
[20] P. Ajith, M. Hannam, S. Husa, Y. Chen, B. Bruegmann, *et al.*, Phys.Rev.Lett. **106**, 241101 (2011), arXiv:0909.2867 [gr-qc].
[21] T. Damour, A. Nagar, and M. Trias, Phys.Rev. **D83**, 024006 (2011), arXiv:1009.5998 [gr-qc].
[22] L. Santamaría, F. Ohme, P. Ajith, B. Bruegmann, N. Dorband, *et al.*, Phys.Rev. **D82**, 064016 (2010), arXiv:1005.3306 [gr-qc].
[23] A. Taracchini, Y. Pan, A. Buonanno, E. Barausse, M. Boyle, *et al.*, Phys.Rev. **D86**, 024011 (2012), arXiv:1202.0790 [gr-qc].
[24] T. Damour, A. Nagar, and S. Bernuzzi, Phys.Rev. **D87**, 084035 (2012), arXiv:1212.4357 [gr-qc].
[25] F. Ohme, M. Hannam, and S. Husa, Phys.Rev. **D84**, 064029 (2011), arXiv:1107.0996 [gr-qc].
[26] P. Ajith and S. Bose, Phys.Rev. **D79**, 084032 (2009), arXiv:0901.4936 [gr-qc].
[27] S. T. McWilliams, J. I. Thorpe, J. G. Baker, and B. J. Kelly, Phys.Rev. **D81**, 064014 (2010), arXiv:0911.1078 [gr-qc].
[28] S. T. McWilliams, B. J. Kelly, and J. G. Baker, Phys.Rev. **D82**, 024014 (2010), arXiv:1004.0961 [gr-qc].
[29] P. Amaro-Seoane, S. Aoudia, S. Babak, P. Binetruy, E. Berti, *et al.*, (2012), arXiv:1201.3621 [astro-ph.CO].
[30] P. Amaro-Seoane, S. Aoudia, S. Babak, P. Binetruy, E. Berti, *et al.*, Class.Quant.Grav. **29**, 124016 (2012), arXiv:1202.0839 [gr-qc].
[31] S. Bose, S. Ghosh, and A. Parameswaran, (2012), arXiv:1207.3361 [gr-qc].
[32] T. B. Littenberg, J. G. Baker, A. Buonanno, and B. J. Kelly, (2012), arXiv:1210.0893 [gr-qc].
[33] L. Baiotti, T. Damour, B. Giacomazzo, A. Nagar, and L. Rezzolla, Phys.Rev. **D84**, 024017 (2011), arXiv:1103.3874 [gr-qc].
[34] S. Bernuzzi, M. Thierfelder, and B. Bruegmann, Phys.Rev. **D85**, 104030 (2012), arXiv:1109.3611 [gr-qc].
[35] S. Bernuzzi, A. Nagar, M. Thierfelder, and B. Brugmann, Phys.Rev. **D86**, 044030 (2012), arXiv:1205.3403 [gr-qc].
[36] K. Hotokezaka, K. Kyutoku, and M. Shibata, (2013), arXiv:1301.3555 [gr-qc].
[37] E. Berti, S. Iyer, and C. M. Will, Phys.Rev. **D77**, 024019 (2008), arXiv:0709.2589 [gr-qc].
[38] A. H. Nitz, A. Lundgren, D. A. Brown, E. Ochsner, D. Keppel, *et al.*, (2013), arXiv:1307.1757 [gr-qc].
[39] I. Harry, A. Nitz, D. A. Brown, A. Lundgren, E. Ochsner, *et al.*, (2013), arXiv:1307.3562 [gr-qc].
[40] H.-S. Cho, E. Ochsner, R. O'Shaughnessy, C. Kim, and C.-H. Lee, Phys.Rev. **D87**, 024004 (2013), arXiv:1209.4494 [gr-qc].
[41] K. Kyutoku, M. Shibata, and K. Taniguchi, Phys.Rev. **D82**, 044049 (2010), arXiv:1008.1460 [astro-ph.HE].
[42] L. Rezzolla, P. Diener, E. N. Dorband, D. Pollney, C. Reisswig, E. Schnetter, and J. Seiler, Astrophys. J. **674**, L29 (2008), arXiv:0710.3345.
[43] E. Berti, V. Cardoso, and C. M. Will, Phys. Rev. D **73**, 064030 (2006).
[44] F. Foucart, Phys.Rev. **D86**, 124007 (2012), arXiv:1207.6304 [astro-ph.HE].
[45] L. G. Fishbone, Astrophys. J. **185**, 43 (1973).
[46] J. M. Bardeen, W. H. Press, and S. A. Teukolsky, Astrophys.J. **178**, 347 (1972).
[47] F. Pannarale, ArXiv e-prints (2012), arXiv:1208.5869 [gr-qc].
[48] J. S. Read, B. D. Lackey, B. J. Owen, and J. L. Friedman, Phys.Rev. **D79**, 124032 (2009), arXiv:0812.2163 [astro-ph].
[49] P. Demorest, T. Pennucci, S. Ransom, M. Roberts, and J. Hessels, Nature **467**, 1081 (2010), arXiv:1010.5788 [astro-ph.HE].
[50] J. Antoniadis, P. C. Freire, N. Wex, T. M. Tauris, R. S. Lynch, *et al.*, Science **340**, 6131 (2013), arXiv:1304.6875 [astro-ph.HE].
[51] L. Baiotti, T. Damour, B. Giacomazzo, A. Nagar, and L. Rezzolla, Phys.Rev.Lett. **105**, 261101 (2010),

TABLE IV. Coefficients of the fit in Eq. (B1) for the total noise data of the three KAGRA configurations considered in this paper: varBRSE (KAGRA variable configuration in broadband mode); maxBRSE (KAGRA in broadband mode, optimized for BNS inspiral detection); varDRSE (KAGRA variable configuration in detuned mode). $f_0 = 84.3335\,\mathrm{Hz}$ for varBRSE and maxBRSE, and $f_0 = 83.3681\,\mathrm{Hz}$ for varDRSE (see text). The noise data for KAGRA is available at the KAGRA webpage [3].

KAGRA	s_0 $[10^{-47}\,\mathrm{Hz}^{-1}]$	a_2	a_1	b_{05}	b_1	b_2	b_3	b_4	b_5	b_{16} $[10^{-15}]$
varBRSE	1.20522	0.0653054	0.00563030	0.535848	0.109784	−0.885726	0.160197	0.300831	0.0350983	5.97876
maxBRSE	1.25262	0.108905	−0.000260438	−1.27327	2.74441	−2.71327	0.759074	0.354601	0.0389407	5.41997
varDRSE	1.13778	0.135200	−0.0194294	−9.81375	17.3277	−10.8376	2.17689	0.889623	0.0510381	7.17394

arXiv:1009.0521 [gr-qc].

[52] K. Kyutoku, H. Okawa, M. Shibata, and K. Taniguchi, Phys.Rev. **D84**, 064018 (2011), arXiv:1108.1189 [astro-ph.HE].

[53] E. Berti, V. Cardoso, and C. M. Will, AIP Conf.Proc. **848**, 687 (2006), arXiv:gr-qc/0601077 [gr-qc].

[54] F. Ozel, Nature (2006), arXiv:astro-ph/0605106 [astro-ph].

[55] C. Cutler and E. E. Flanagan, Phys.Rev. **D49**, 2658 (1994), arXiv:gr-qc/9402014 [gr-qc].

[56] E. Poisson and C. M. Will, Phys.Rev. **D52**, 848 (1995), arXiv:gr-qc/9502040 [gr-qc].

[57] P. Ajith, Phys.Rev. **D84**, 084037 (2011), arXiv:1107.1267 [gr-qc].

[58] Base sensitivities - ET workarea, `https://workarea.et-gw.eu/et/WG4-Astrophysics/base-sensitivity` (2013).

[59] M. Vallisneri, Phys.Rev.Lett. **84**, 3519 (2000), arXiv:gr-qc/9912026 [gr-qc].

[60] V. Ferrari, L. Gualtieri, and F. Pannarale, Classical Quantum Gravity **26**, 125004 (2009), arXiv:0801.2911.

[61] V. Ferrari, L. Gualtieri, and F. Pannarale, Phys.Rev. **D81**, 064026 (2010), arXiv:0912.3692 [gr-qc].

[62] K. Taniguchi, T. W. Baumgarte, J. A. Faber, and S. L. Shapiro, Phys. Rev. D **77**, 044003 (2008), arXiv:0710.5169 [gr-qc].

[63] M. Shibata, K. Kyutoku, T. Yamamoto, and K. Taniguchi, Phys. Rev. D **79**, 044030 (2009), arXiv:0902.0416 [gr-qc].

[64] F. Pannarale, L. Rezzolla, F. Ohme, and J. S. Read, Phys.Rev. **D84**, 104017 (2011), 4 pages, 4 figures, arXiv:1103.3526 [astro-ph.HE].

[65] Online Mathematica code, `http://www.phy.olemiss.edu/~berti/research.html` (2013).

[66] F. Foucart, M. D. Duez, L. E. Kidder, and S. A. Teukolsky, Phys.Rev. **D83**, 024005 (2011), arXiv:1007.4203 [astro-ph.HE].

[67] F. Foucart, M. B. Deaton, M. D. Duez, L. E. Kidder, I. MacDonald, *et al.*, Phys.Rev. **D87**, 084006 (2013), arXiv:1212.4810 [gr-qc].

[68] D. Radice, L. Rezzolla, and F. Galeazzi, (2013), arXiv:1306.6052 [gr-qc].